



# Strong Ground Motion in the 2011 Tohoku Earthquake: A One-Directional Three-Component Modeling

Maria Paola Santisi d'Avila, Jean François Semblat, Luca Lenti

► **To cite this version:**

Maria Paola Santisi d'Avila, Jean François Semblat, Luca Lenti. Strong Ground Motion in the 2011 Tohoku Earthquake: A One-Directional Three-Component Modeling. Bulletin of the Seismological Society of America, Seismological Society of America, 2013, 103 (2B), pp.1394-1410. <10.1785/0120120208>. <hal-00850829>

**HAL Id: hal-00850829**

**<https://hal.archives-ouvertes.fr/hal-00850829>**

Submitted on 9 Aug 2013

**HAL** is a multi-disciplinary open access archive for the deposit and dissemination of scientific research documents, whether they are published or not. The documents may come from teaching and research institutions in France or abroad, or from public or private research centers.

L'archive ouverte pluridisciplinaire **HAL**, est destinée au dépôt et à la diffusion de documents scientifiques de niveau recherche, publiés ou non, émanant des établissements d'enseignement et de recherche français ou étrangers, des laboratoires publics ou privés.

1 **Strong Ground Motion in the 2011 Tohoku Earthquake:**

2 **a 1Directional - 3Component Modeling**

3

4 by Maria Paola Santisi d'Avila, Jean-François Semblat and Luca Lenti

5

6

7

8

9

10

11 Corresponding author:

12 Maria Paola Santisi d'Avila

13 University of Nice Sophia Antipolis - Laboratoire Jean Alexandre Dieudonné

14

15 Address:

16 14bis, Rue François Guisol - 06300 Nice - France

17 Phone: +33(0)4 92 07 69 96

18 Email: msantisi@unice.fr

19 mpaolasantisi@gmail.com

20

21

22

23

24 **ABSTRACT**

25 Local wave amplification due to strong seismic motions in surficial multilayered soil is  
26 influenced by several parameters such as the wavefield polarization and the dynamic properties  
27 and impedance contrast between soil layers. The present research aims at investigating seismic  
28 motion amplification in the 2011 Tohoku earthquake through a one-directional three-component  
29 (1D-3C) wave propagation model. A 3D nonlinear constitutive relation for dry soils under cyclic  
30 loading is implemented in a quadratic line finite element model. The soil rheology is modeled by  
31 mean of a multi-surface cyclic plasticity model of the Masing-Prandtl-Ishlinskii-Iwan (MPII)  
32 type. Its major advantage is that the rheology is characterized by few commonly measured  
33 parameters. Ground motions are computed at the surface of soil profiles in the Tohoku area  
34 (Japan) by propagating 3C signals recorded at rock outcrops, during the 2011 Tohoku  
35 earthquake. Computed surface ground motions are compared to the Tohoku earthquake records  
36 at alluvial sites and the reliability of the 1D-3C model is corroborated. The 1D-3C approach is  
37 compared with the combination of three separate one-directional analyses of one motion  
38 component propagated independently (1D-1C approach). The 3D loading path due to the 3C-  
39 polarization leads to multiaxial stress interaction that reduces soil strength and increases  
40 nonlinear effects. Time histories and spectral amplitudes, for the Tohoku earthquake, are  
41 numerically reproduced. The 1D-3C approach allows the evaluation of various parameters of the  
42 3C motion and 3D stress and strain evolution all over the soil profile.

43

44 **INTRODUCTION**

45 One-directional wave propagation analyses are an easy way to estimate the surface ground  
46 motion, even in the case of strong seismic events. Seismic waves due to strong ground motions

47 propagating in surficial soil layers may both reduce soil stiffness and increase nonlinear effects.  
48 The nonlinear behavior of the soil may have beneficial or detrimental effects on the dynamic  
49 response at the surface, depending on the energy dissipation rate. The three-dimensional (3D)  
50 loading path also influences the stresses into the soil and thus its seismic response.

51 The recent records of the 9 Mw 11 March 2011 Tohoku earthquake, in Japan, allow to  
52 understand the influence of incident wave polarization. This event is one of the largest  
53 earthquakes in the world that has been well recorded in the near-fault zone. According to the  
54 Japanese database of the K-Net accelerometer network (see Data and Resources Section), the  
55 main feature of the Tohoku three-component records is that the vertical to maximum horizontal  
56 component ratio appears close to one for several soil profiles and the peak vertical motion can  
57 locally be higher than the minor horizontal component of ground motion. This is an interesting  
58 observation because earthquake vertical component was neglected in structural design codes in  
59 the recent past. The vertical to horizontal ratio, previously considered trivial, becomes essential  
60 to characterize 3D loading effects and multiaxial stress interaction in strong ground motion  
61 modeling.

62 In order to investigate site-specific seismic hazard, past studies have been devoted to one-  
63 directional shear wave propagation in a multilayered soil profile (1D-propagation) considering  
64 one motion component only (1C-polarization). Several one-directional models and related codes  
65 were developed, to investigate one-component ground response of horizontally layered sites,  
66 reproducing soil behavior as equivalent linear (SHAKE, Schnabel *et al.*, 1972; EERA, Bardet *et*  
67 *al.*, 2000), dry nonlinear (NERA, Bardet *et al.*, 2001) and saturated nonlinear (DESRA-2, Lee  
68 and Finn, 1978).

69 Soils are complex materials and a linear approach is not reliable to model their seismic response

70 to strong earthquakes. The continuous improvement of dynamic test apparatus allows to  
71 measure dynamic soil properties over a wide range of strains, showing the highly nonlinear  
72 deformation characteristics of soil and the significant variation of shear modulus and damping  
73 ratio with the amplitude of shear strain under cyclic loading (Seed and Idriss, 1970a; Hardin and  
74 Drnevich, 1972a, 1972b; Kim and Novak, 1981; Lefebvre *et al.*, 1989; Vucetic and Dobry,  
75 1991; Vucetic, 1994; Ishihara, 1996; Hsu and Vucetic, 2004, 2006). At larger strain levels, the  
76 nonlinearity may reduce the shear modulus and increase the damping. Observations in situ  
77 enabled to undertake quantitative studies on the nonlinear response of soft sedimentary sites and  
78 to evaluate local site effects (Seed and Idriss, 1970b; Satoh *et al.*, 1995; Bonilla *et al.*, 2002; De  
79 Martin *et al.*, 2010).

80 A nonlinear site response analysis accounting for hysteresis allows to follow the time evolution  
81 of the stress and strain during seismic events and to estimate the resulting surface seismic  
82 ground motion at large strain levels. The nonlinear analysis requires the propagation of a seismic  
83 wave in a nonlinear medium by using an appropriate constitutive model and integrating the  
84 wave equation in the time domain. Inputs to these analyses include acceleration time histories at  
85 bedrock and nonlinear material properties of the various soil strata underlying the site. The main  
86 difficulty in nonlinear analysis is to find a constitutive model that reproduces faithfully the  
87 nonlinear and hysteretic behavior of soil under cyclic loadings, with the minimum number of  
88 parameters.

89 Considering the 3D loading path means representing the 3D hysteretic behavior of soils, which  
90 is difficult to model because the yield surface may present a complex form. The nonlinear 3D  
91 constitutive behavior depends on the 3D loading path. The three motion components are  
92 coupled, due to the nonlinear 3D constitutive behavior, and they cannot be computed separately

93 (Li *et al.*, 1992; Santisi d'Avila *et al.*, 2012). Li (1990) incorporated the three-dimensional  
94 cyclic plasticity soil model proposed by Wang *et al.* (1990) in a 1D finite element procedure  
95 (SUMDES code, Li *et al.*, 1992), in terms of effective stress, to simulate the one-directional  
96 wave propagation accounting for pore pressure in the soil. However, this complex rheology  
97 needs an excessive number of parameters to characterize the soil model.

98 In the present research, the nonlinear soil behavior is represented by the so-called Masing-  
99 Prandtl-Ishlinskii-Iwan (MPII) model, according to (Segalman and Starr, 2008), or Iwan's model  
100 (Iwan, 1967). It is a multi-surface plasticity mechanism for cyclic loading and it depends on few  
101 parameters that can be obtained from ordinary laboratory tests. Material properties include the  
102 dynamic shear modulus at low strain and the variation of shear modulus with shear strain. This  
103 rheology allows the dry soil to develop large strains in the range of stable nonlinearity, where the  
104 shape of hysteresis loops remains unvaried in the time. Due to its three-directional nature, the  
105 procedure can handle both shear wave and compression wave simultaneously and predict not  
106 only horizontal motion but vertical settlement too.

107 The implementation of the MPII nonlinear cyclic constitutive model in a finite element scheme  
108 (SWAP\_3C code) is presented in detail by Santisi d'Avila *et al.* (2012). The authors analyze the  
109 importance of a three-directional shaking problem, evaluating the seismic ground motion due to  
110 three-component strong earthquakes, for well-known stratigraphies, using synthetic incident  
111 wavelets. The role of critical parameters affecting the soil response is investigated. The main  
112 feature of the procedure is that it solves the specific three-dimensional stress-strain problem for  
113 seismic wave propagation along one-direction only, using a constitutive behavior depending only  
114 on commonly measured soil properties.

115 In the present research, the goal is to assess the reliability of the model proposed by the authors

116 (Santisi d'Avila *et al.*, 2012) and confirm, through actual data, the findings of the parametric  
117 analysis previously done using synthetic wavelets. It was observed that the shear modulus  
118 decreases and the dissipation increases, for a given maximum strain amplitude, from one to three  
119 component unidirectional propagated wave. The material strength is lower under triaxial loading  
120 rather than for simple shear loading. The shape of hysteresis loops remains unvaried in the time,  
121 for one-component loading, in the strain range of stable nonlinearity. In the case of three-  
122 component loading, the shape of the hysteresis loops changes in the time for shear strains in the  
123 same range. Hysteresis loops for each horizontal direction are altered as a consequence of the  
124 interaction between loading components. The main difference between three superimposed one-  
125 component ground motions (1D-1C approach) and the proposed one-directional three-  
126 component propagation model (1D-3C approach) is remarkable in terms of ground motion time  
127 history, maximum stress and hysteretic behavior, with more nonlinearity and coupling effects  
128 between components. This kind of consequence is more evident with decreasing seismic  
129 velocity ratio in the soil and increasing vertical to horizontal component ratio of the incident  
130 wave.

131 The 1D-3C propagation model and the main features of the applied constitutive relation are  
132 presented. The validation of the 1D-3C approach is undertaken comparing the three-component  
133 records of the 2011 Tohoku earthquake with numerical time histories. Seismic records with  
134 vertical to horizontal acceleration ratio higher than 70 % are applied to investigate the impact of  
135 a large vertical to horizontal peak acceleration ratio. The simultaneous propagation of a three  
136 component input signal, in a system of horizontal soil layers, is studied using the proposed  
137 model. The case of three components simultaneously propagated (1D-3C) is compared with that  
138 of three superimposed one-component ground motions (1D-1C), to understand the influence of a

139 3D loading path and input wavefield polarization. The influence of the soil properties and quake  
140 features on the local seismic response is discussed for the case of multilayered soil profiles in  
141 the Tohoku area (Japan).

142

### 143 **ONE-DIRECTIONAL THREE-COMPONENT PROPAGATION MODEL**

144 The three components of the seismic motion are propagated along one direction in a nonlinear  
145 soil profile from the top of the underlying elastic bedrock. The multilayered soil is assumed  
146 infinitely extended along the horizontal directions. Shear and pressure waves propagate  
147 vertically in the  $z$ -direction. These hypotheses yield no strain variation in  $x$ - and  $y$ -direction.  
148 At a given depth, soil is assumed to be a continuous and homogeneous medium.  
149 Transformations remain small during the process and the cross sections of three-dimensional  
150 soil elements remain planes.

151

#### 152 **Spatial discretization**

153 Soil stratification is discretized into a system of horizontal layers, parallel to the  $xy$  plane, by  
154 using a finite element scheme (Fig. 1). Quadratic line elements with three nodes are considered.  
155 According to the finite element modeling, the discrete form of equilibrium equations, is  
156 expressed in the matrix form as

$$157 \quad \mathbf{M}\ddot{\mathbf{D}} + \mathbf{C}\dot{\mathbf{D}} + \mathbf{F}_{\text{int}} = \mathbf{F} \quad (1)$$

158 where  $\mathbf{M}$  is the mass matrix,  $\dot{\mathbf{D}}$  and  $\ddot{\mathbf{D}}$  are velocity and acceleration vectors, respectively, i.e.  
159 the first and second time derivatives of the displacement vector  $\mathbf{D}$ .  $\mathbf{F}_{\text{int}}$  is the vector of nodal  
160 internal forces and  $\mathbf{F}$  is the load vector.  $\mathbf{C}$  is a damping matrix derived from the chosen  
161 absorbing boundary condition. The differential equilibrium problem (1) is solved according to



162 compatibility conditions and the hypothesis of no strain variation in the horizontal directions, to  
163 a three-dimensional nonlinear constitutive relation for cyclic loading and the boundary  
164 conditions described below.

165 Discretizing the soil column into  $n_e$  quadratic line elements and consequently into  $n = 2n_e + 1$   
166 nodes (Fig. 1), having three translational degrees of freedom each, yields a  $3n$ -dimensional  
167 displacement vector  $\mathbf{D}$  composed by three blocks whose terms are the displacement of the  $n$   
168 nodes in  $x$ -,  $y$ - and  $z$ -direction, respectively. Soil properties are assumed constant in each  
169 finite element and soil layer.

170 The minimum number of quadratic line elements per layer  $n_e^j$  is defined considering that  $p = 10$   
171 is the minimum number of nodes per wavelength to accurately represent the seismic signal  
172 (Kuhlemeyer and Lysmer, 1973; Semblat and Brioist, 2000) and it is evaluated as

$$173 \quad \min n_e^j = \frac{H_j}{2} \frac{p f}{v_s} \quad (2)$$

174 where  $H_j$  is the thickness of layer  $j$  (Fig. 1),  $f$  is the assumed maximum frequency of the  
175 input signal and  $v_s$  is the assumed minimum shear velocity in the medium. The seismic signal  
176 wavelength is equal to  $v_s/f$ . The assumed minimum  $v_s$  is related to the assumed maximum  
177 shear modulus decay and allows to account for non linearities. In this study,  $v_s$  corresponds to a  
178 70% reduction of the initial shear modulus. The maximum frequency  $f$ , used to assess the  
179 minimum number of elements per layer  $n_e^j$ , is assumed to be 15 Hz as an accurate choice.

180 The assemblage of  $(3n \times 3n)$ -dimensional matrices and  $3n$ -dimensional vectors is independently  
181 done for each of the three  $(n \times n)$ -dimensional submatrices and  $n$ -dimensional subvectors,  
182 respectively, corresponding to  $x$ -,  $y$ - and  $z$ -direction of motion.

183 **Boundary conditions**

184 The system of horizontal soil layers is bounded at the top by the free surface and at the bottom  
185 by a semi-infinite elastic medium representing the seismic bedrock. The stresses normal to the  
186 free surface are assumed null and the following condition, implemented by Joyner and Chen  
187 (1975) and Joyner (1975) in a finite difference formulation and used by Bardet and Tobita  
188 (2001) in NERA code, is applied at the soil-bedrock interface to take into account the finite  
189 rigidity of the bedrock:

190 
$$-\mathbf{p}^T \boldsymbol{\sigma} = \mathbf{c}(\mathbf{v} - 2\mathbf{v}_b) \quad (3)$$

191 The stresses normal to the soil column base at the bedrock interface are  $\mathbf{p}^T \boldsymbol{\sigma}$  and  $\mathbf{c}$  is a  $(3 \times 3)$   
192 diagonal matrix whose terms are  $\rho_b v_{sb}$ ,  $\rho_b v_{sb}$  and  $\rho_b v_{pb}$ . The parameters  $\rho_b$ ,  $v_{sb}$  and  $v_{pb}$  are  
193 the bedrock density and shear and pressure wave velocities in the bedrock, respectively. The  
194 three terms of vector  $\mathbf{v}$  are the unknown velocities in  $x$ -,  $y$ - and  $z$ -direction, respectively, at  
195 the interface soil-bedrock (node 1 in Fig. 1). The terms of the 3-dimensional vector  $\mathbf{v}_b$  are the  
196 input bedrock velocities, in the underlying elastic medium in directions  $x$ ,  $y$  and  $z$ ,  
197 respectively. Boundary condition (3) allows energy to be radiated back into the underlying  
198 medium.

199 The three-component bedrock velocity can be obtained by halving seismic records at  
200 outcropping bedrock. The incident bedrock waves are the half of outcropping seismic waves  
201 (Fig. 1), due to the free surface effect in linear elastic medium such as rock.

202 If borehole records are used, the halving operation is not necessary, because records are applied  
203 as incident bedrock signals. The bedrock is assumed elastic in the proposed model, with  
204 absorption and reflection of waves at the soil-bedrock interface, according to equation (3).  
205 However, the borehole input signal contains incident and reflected waves. The absorbing

206 condition in equation (3) is commonly used also when borehole records are applied (NERA  
 207 code, Bardet and Tobita, 2001), but an imposed motion at the soil-bedrock interface (first node)  
 208 would more properly represent the borehole boundary condition. The implementation of such a  
 209 boundary condition, adopted when borehole records are analyzed, will be a future improvement  
 210 of the proposed procedure.

211

### 212 **Time discretization**

213 The finite element model and the soil nonlinearity require spatial and time discretization,  
 214 respectively, to permit the problem solution (Hughes, 1987; Crisfield, 1991). The rate type  
 215 constitutive relation between stress and strain is linearized at each time step. Accordingly,  
 216 equation (1) is expressed as

$$217 \quad \mathbf{M} \Delta \ddot{\mathbf{D}}_k^i + \mathbf{C} \Delta \dot{\mathbf{D}}_k^i + \mathbf{K}_k^i \Delta \mathbf{D}_k^i = \Delta \mathbf{F}_k \quad (4)$$

218 where the subscript  $k$  indicates the time step  $t_k$  and  $i$  the iteration of the problem solving  
 219 process, as explained below.

220 The step-by-step process is solved by the Newmark algorithm, expressed as follows:

$$221 \quad \begin{cases} \Delta \dot{\mathbf{D}}_k^i = \frac{\gamma}{\beta \Delta t} \Delta \mathbf{D}_k^i - \frac{\gamma}{\beta} \dot{\mathbf{D}}_{k-1} + \left(1 - \frac{\gamma}{2\beta}\right) \Delta t \ddot{\mathbf{D}}_{k-1} \\ \Delta \ddot{\mathbf{D}}_k^i = \frac{1}{\beta \Delta t^2} \Delta \mathbf{D}_k^i - \frac{1}{\beta \Delta t} \dot{\mathbf{D}}_{k-1} - \frac{1}{2\beta} \ddot{\mathbf{D}}_{k-1} \end{cases} \quad (5)$$

222 The Newmark's procedure is an implicit self-starting unconditionally stable approach for one-  
 223 step time integration in dynamic problems (Newmark, 1959; Hilber *et al.*, 1977; Hughes, 1987).

224 The two parameters  $\beta=0.3025$  and  $\gamma=0.6$  guarantee unconditional stability of the time  
 225 integration scheme and numerical damping properties to damp higher modes (Hughes, 1987).

226 Equations (4) and (5) yield

227 
$$\bar{\mathbf{K}}_k^i \Delta \mathbf{D}_k^i = \Delta \mathbf{F}_k + \mathbf{A}_{k-1} \quad (6)$$

228 where the modified stiffness matrix is defined as

229 
$$\bar{\mathbf{K}}_k^i = \frac{1}{\beta \Delta t^2} \mathbf{M} + \frac{\gamma}{\beta \Delta t} \mathbf{C} + \mathbf{K}_k^i \quad (7)$$

230 and  $\mathbf{A}_{k-1}$  is a vector depending on the response in previous time step, given by

231 
$$\mathbf{A}_{k-1} = \left[ \frac{1}{\beta \Delta t} \mathbf{M} + \frac{\gamma}{\beta} \mathbf{C} \right] \dot{\mathbf{D}}_{k-1} + \left[ \frac{1}{2\beta} \mathbf{M} + \left( \frac{\gamma}{2\beta} - 1 \right) \Delta t \mathbf{C} \right] \ddot{\mathbf{D}}_{k-1} \quad (8)$$

232 Equation (4) requires an iterative solving, at each time step  $k$ , to correct the tangent stiffness  
 233 matrix  $\mathbf{K}_k^i$ . Starting from the stiffness matrix  $\mathbf{K}_k^1 = \mathbf{K}_{k-1}$ , evaluated at the previous time step, the  
 234 value of matrix  $\mathbf{K}_k^i$  is updated at each iteration  $i$  (Crisfield, 1991). After evaluating the  
 235 displacement increment  $\Delta \mathbf{D}_k^i$  by equation (6), using the tangent stiffness matrix corresponding to  
 236 the previous time step, velocity and acceleration increments can be estimated through equation  
 237 (5) and the total motion is obtained according to

238 
$$\mathbf{D}_k^i = \mathbf{D}_{k-1} + \Delta \mathbf{D}_k^i \quad \dot{\mathbf{D}}_k^i = \dot{\mathbf{D}}_{k-1} + \Delta \dot{\mathbf{D}}_k^i \quad \ddot{\mathbf{D}}_k^i = \ddot{\mathbf{D}}_{k-1} + \Delta \ddot{\mathbf{D}}_k^i \quad (9)$$

239 where  $\mathbf{D}_k^i$ ,  $\dot{\mathbf{D}}_k^i$  and  $\ddot{\mathbf{D}}_k^i$  are the vectors of total displacement, velocity and acceleration,  
 240 respectively. The strain increments are then derived from the displacement increments, terms of  
 241 vector  $\Delta \mathbf{D}_k^i$ . Stress increments and tangent constitutive matrix are obtained through the assumed  
 242 constitutive relationship. Gravity load is imposed as static initial condition in terms of strain and  
 243 stress at nodes. The modified stiffness matrix  $\bar{\mathbf{K}}_k^i$  is calculated and the process restarts. The  
 244 correction process continues until the difference between two successive approximations is  
 245 reduced to a fixed tolerance, according to

246 
$$\left| \mathbf{D}_k^i - \mathbf{D}_k^{i-1} \right| < \alpha \left| \mathbf{D}_k^i \right| \quad (10)$$

247 where  $\alpha = 10^{-3}$  (Mestat, 1993, 1998). Afterwards, the next time step is analyzed.

248

## 249 **FEATURES OF THE 3D NONLINEAR HYSTERETIC MODEL**

250 The three-dimensional constitutive model for soil used to model the propagation of a three-  
251 component earthquake, in stratified soils, is a Masing-Prandtl-Ishlinskii-Iwan (MPII) type  
252 constitutive model (Segalman and Starr, 2008), suggested by Iwan (1967) and applied by Joyner  
253 (1975) and Joyner and Chen (1975) in a finite difference formulation. It is used in the present  
254 work to properly model the nonlinear soil behavior in a finite element scheme (Santisi d'Avila *et*  
255 *al.*, 2012).

256 The so-called Masing rules, presented in 1926, describe the loading and unloading paths in the  
257 stress-strain space, reproducing quite faithfully the hysteresis observed in the laboratory. Prandtl  
258 proposed, in 1928, an elasto-plastic model with strain-hardening, re-examined by Ishlinskii in  
259 1944, obtained by coupling a family of stops in parallel or of plays in series (Bertotti and  
260 Mayergoyz, 2006). Iwan (1967) proposed an extension of the standard incremental theory of  
261 plasticity (Fung, 1965), by introducing a family of yield surfaces, modifying the 1D approach  
262 with a single yield surface in the stress space. He modeled nonlinear stress-strain curves using a  
263 series of mechanical elements, having decreasing stiffnesses and increasing sliding resistance.  
264 The MPII model takes into account the nonlinear hysteretic behavior of soils in a three-  
265 dimensional stress state, using an elasto-plastic approach with hardening, based on the definition  
266 of a series of nested yield surfaces, according to von Mises' criterion. The MPII model is used to  
267 represent the behavior of materials satisfying Masing criterion (Kramer, 1996) and not  
268 depending on the number of loading cycles. The stress level depends on the strain increment and  
269 strain history but not on the strain rate. Therefore, this rheological model has no viscous damping

270 and the energy dissipation process is purely hysteretic and does not depend on the frequency.  
 271 Shear modulus and damping ratio are strain-dependent.  
 272 The main feature of the MPII rheological model is that the only necessary input data, to identify  
 273 soil properties in the applied constitutive model, is the shear modulus decay curve  $G(\gamma)$  versus  
 274 shear strain  $\gamma$ . The initial elastic shear modulus  $G_0 = \rho v_s^2$ , measured at the elastic behavior range  
 275 limit  $\gamma \cong 0.001\%$  (Fahey, 1992), depends on the mass density  $\rho$  and the shear wave velocity in  
 276 the medium  $v_s$ . The P-wave modulus  $M = \rho v_p^2$ , depending on the pressure wave velocity in the  
 277 medium  $v_p$ , characterizes the longitudinal behavior of soil. The seismic velocity ratio  
 278 (compressional to shear wave velocity ratio  $v_p/v_s$ ), evaluated by

$$279 \quad \left(v_p/v_s\right)^2 = 2(1-\nu)/(1-2\nu) \quad (11)$$

280 is a function of the Poisson's ratio  $\nu$ . This is a parameter of the constitutive behavior for  
 281 multiaxial load and of the interaction between components in the three-dimensional response.

282 The MPII hysteretic model for dry soils, used in the present research, is applied for strains in the  
 283 range of stable nonlinearity. In this range, where the shear strain is lower than the stability  
 284 threshold (Lefebvre *et al.*, 1989), both shear modulus and damping ratio do not depend on the  
 285 number of cycles. Stable stress-strain cycles are observed, for which the shape of hysteresis  
 286 loops remains unvaried at each cycle, for one-component loading. When the stability threshold is  
 287 overtaken, the soil mechanical response changes at each cycle and both shear modulus and  
 288 damping ratio vary abruptly (Zambelli *et al.*, 2006). Unstable liquefaction phenomena appear for  
 289 large shear strains and, consequently, both the hysteresis loop shape and the average shear  
 290 stiffness evolve progressively with the number of cycles.

291 Large strain rates are not adequately reproduced without taking into account undrained condition

292 for soils. Constitutive behavior models for saturated soils would allow to attain larger strains  
 293 with proper accuracy. It is the reason why the shear modulus decay is accepted until 70 %,  
 294 corresponding to the minimum shear velocity in the soil in equation (2), used to obtain an  
 295 appropriate space discretization.

296 In the present study the soil behavior is assumed adequately described by a hyperbolic stress-  
 297 strain curve (Hardin and Drnevich, 1972b). This assumption yields a normalized shear modulus  
 298 decay curve, used as input curve representing soil characteristics, expressed as

$$299 \quad G/G_0 = 1/(1+|\gamma/\gamma_r|) \quad (12)$$

300 where  $\gamma_r$  is a reference shear strain corresponding to an actual tangent shear modulus equivalent  
 301 to 50 % of the initial shear modulus, in a normalized shear modulus decay curve provided by  
 302 laboratory test data. The applied constitutive model (Iwan, 1967; Joyner and Chen, 1975; Joyner,  
 303 1975) does not depend on the hyperbolic initial loading curve. It could incorporate also shear  
 304 modulus decay curves obtained from laboratory dynamic tests on soil samples.

305 The stiffness matrix  $\mathbf{K}_k^i$  is deduced, at each time step  $k$  and iteration  $i$ , knowing the tangent  
 306 constitutive matrix  $\mathbf{E}_k^i$ . The actual strain level and the strain and stress values at the previous  
 307 time step allow to evaluate the tangent constitutive (6x6) matrix  $\mathbf{E}_k^i$  and the stress increment,  
 308 according to the incremental constitutive relationship  $\Delta\boldsymbol{\sigma}_k^i = \mathbf{E}_k^i \Delta\boldsymbol{\varepsilon}_k^i$ . The deviatoric constitutive  
 309 matrix  $\mathbf{E}_d$  for a three-dimensional soil element is obtained according to Iwan's procedure, as  
 310 presented by Joyner (1975), and allows to evaluate the vector of deviatoric stress increments  $\Delta\mathbf{s}$ ,  
 311 knowing the vector of deviatoric strain increments  $\Delta\mathbf{e}$ , according to  $\Delta\mathbf{s} = \mathbf{E}_d \Delta\mathbf{e}$ . The total  
 312 constitutive matrix  $\mathbf{E}$  is evaluated starting from  $\mathbf{E}_d$  (Santisi d'Avila *et al.*, 2012).

313 Stress and strain rate in the one-dimensional (1D) soil profile due to the propagation of a three-

314 component earthquake are expressed in the following analysis in terms of octahedral shear stress  
315 and strain, accounting for the hypothesis of infinite horizontal soil ( $\varepsilon_{xx} = 0, \varepsilon_{yy} = 0, \gamma_{xy} = 0$ ).  
316 According to the 3D constitutive model and for null  $\gamma_{xy}$ , the only null stress component is the  
317 in-plane shear stress  $\tau_{xy}$ . Octahedral stress (respectively strain) is chosen to combine the three-  
318 dimensional stress (respectively strain) components in a unique scalar parameter, that allows an  
319 adequate comparison of the simultaneous propagation of the three motion components (1D-3C)  
320 and the independent propagation of the three components (1D-1C) superposed a posteriori. The  
321 1D-1C approach is a good approximation in the case of low strains within the linear range  
322 (superposition principle, Oppenheim *et al.*, 1997). The effects of axial-shear stress interaction in  
323 multiaxial stress states have to be taken into account for higher strain rates, in the nonlinear  
324 range. The octahedral stress and strain are respectively obtained by

$$\begin{aligned}
\tau_{oct} &= \frac{1}{3} \sqrt{(\sigma_{xx} - \sigma_{yy})^2 + (\sigma_{yy} - \sigma_{zz})^2 + (\sigma_{zz} - \sigma_{xx})^2 + 6(\tau_{yz}^2 + \tau_{zx}^2)} \\
\gamma_{oct} &= \frac{2}{3} \sqrt{2(\varepsilon_{zz})^2 + 6(\varepsilon_{yz}^2 + \varepsilon_{zx}^2)}
\end{aligned}
\tag{13}$$

326

### 327 **VALIDATION OF THE 1D-3C WAVE PROPAGATION MODELING**

328 Recorded data from the 9 Mw 11 March 2011 Tohoku earthquake by the K-Net and KiK-Net  
329 accelerometer networks have been analyzed in this research (see Data and Resources Section), to  
330 numerically reproduce the surface ground motion and to provide non-measured parameters.  
331 Kyoshin Network (K-Net) database stores ground motion records at the surface of soil profiles  
332 and related stratigraphies; whereas, the Kiban-Kyoshin Network (KiK-Net) database provides  
333 surface and borehole seismic records for different stratigraphies.

334 We use records at the surface of alluvial soil profiles to validate the numerical surface ground



335 motion computed by the proposed model. Some rock type profiles close to each analyzed soil  
336 profile are selected (Fig. 2), in the K-Net database (see Data and Resources Section), to get  
337 incident seismic motion at the base of the profiles. Incident seismic motion at the base of soil  
338 profiles is the halved motion at a close outcropping bedrock site (Fig. 1). Incident and surface  
339 seismic motions are known in the case of KiK-Net stratigraphies, according to the assumption  
340 that borehole signals are applied as incident. As explained before, this improper adoption will be  
341 overcome in a later work.

342 The numerical one-directional dynamic response of studied soil profiles is validated by  
343 comparison with recordings in terms of acceleration time histories at the ground surface, since it  
344 is the only available recorded data. The numerical acceleration time history is obtained by the  
345 estimated velocity time history after derivation and low-pass filtering (to 10Hz). The three-  
346 component ground motion is characterized by the modulus which is a unique scalar parameter.  
347 Spectral amplitudes are compared and discussed below.

348

### 349 **Soil profiles**

350 The soil columns modeled in this study, consisting of various layers on seismic bedrock, are  
351 analyzed to validate the 1D-3C wave propagation modeling by using real data and to investigate  
352 the local seismic response by the 1D-3C approach. The stratigraphic setting of four soil profiles  
353 in the Tohoku area (Japan) is used in this analysis (Table 1). The description of the stratigraphy  
354 and lithology of the alluvial deposits in the Tohoku area is provided by the Kyoshin Network  
355 database (see Data and Resources Section). Average shear wave velocities and epicentral  
356 distances are listed in Table 1. The four analyzed soil profiles are in Tohoku area with epicentral  
357 distance up to 400 km and have increasing shear wave velocity with depth. Soil profiles have

358 different properties: depth, number and thickness of layers, soil type and compressional to shear  
359 wave velocity in the soil. Stratigraphies and soil properties used in this analysis are shown in  
360 Tables 2-5. Soil properties are assumed uniform in each layer.

361 The dynamic mechanical properties of the Tohoku alluvial deposits are not provided. The  
362 normalized shear modulus decay curves employed in this work are obtained according to the  
363 hyperbolic model, as in equation (12). The applied reference strain corresponds, for each soil  
364 type in the analyzed profiles, to the 50 % reduction of shear modulus in well-known shear  
365 modulus decay curves of the literature (Tables 2-5). The curve proposed by Seed and Idriss  
366 (1970a) is used to define  $\gamma_r$  for sands and the curve of Seed and Sun (1989) is applied for clays.  
367 A plasticity index in the range of  $PI = 20 - 40$  is assumed in the relationship of Sun *et al.* (1988)  
368 to define  $\gamma_r$  for volcanic ash clay and  $PI = 5 - 10$  is adopted for silt. The reference shear strain  
369 for gravel is defined according to Seed *et al.* (1986). An almost linear behavior is assumed for  
370 stiff layers above the bedrock ( $\gamma_r = 100 \%$ ). The choices of  $\gamma_r$  could influence the analysis, but  
371 the variation in the dynamic response of soil columns is neglected here.

372 The density of soil layers in the profile NIGH11 is not provided by the KiK-Net database, so it is  
373 assumed (Table 5).

374 According to the proposed model, the bedrock has an elastic behavior with a high elastic  
375 modulus. The physical properties assumed for bedrock are the density  $\rho_b = 2100 \text{ kg/m}^3$ , the  
376 shear velocity in the bedrock  $v_{sb} = 1000 \text{ m/s}$  and the pressure wave velocity  $v_{pb}$  is deduced by  
377 (11), by imposing a Poisson's ratio of 0.4. The lack of geotechnical data for deeper layers  
378 induces to assume the bedrock right below the soil profile described by K-Net data.

379

380

381 **Input seismic signals**

382 The four soil profiles have been selected because the vertical to horizontal peak ground  
383 acceleration ratio is higher than 70 % (Table 6), with a low compressional to shear wave velocity  
384 ratio in the soil that implies a low Poisson's ratio, according to equation (11). The minimum  
385  $v_p/v_s$  in each studied stratigraphy is indicated in Table 1. The PGA recorded at the surface of  
386 analyzed soil profiles is slightly higher than the acceleration level commonly used for structural  
387 design in high risk seismic zones. The three components of motion are recorded in North-South  
388 (NS), East-West (EW) and Up-Down (UP) directions, respectively referred to as  $x$ ,  $y$  and  $z$  in  
389 the proposed model. Recorded signals have different polarization. The peak ground acceleration  
390 (PGA) and peak ground velocity (PGV) can be referred (see Table 6) to different directions of  
391 polarization (NS  $\equiv$   $x$  or EW  $\equiv$   $y$ ). PGA and PGV are indicated by bold characters in Table 6. The  
392 three maximum acceleration components, in each direction of motion, correspond to different  
393 times. Maximum acceleration and velocity moduli at the surface of analyzed soil profiles are  
394 listed in Table 6. The waveforms are provided by the Kyoshin Network strong ground motion  
395 database (see Data and Resources Section).

396 Rock type profiles are selected as the sites closest to analyzed soil profiles, where accelerometer  
397 stations are placed and whose stratigraphy is defined as rock, by the K-Net database, all along  
398 the depth, until the surface ground. Rock type profiles have different epicentral distance, depth  
399 and average shear velocity in the soil, as listed in Table 7. The position of soil and rock type  
400 profiles in Tohoku area is shown in Figure 2. A thin surficial soil layer, present in some rock  
401 type profiles (Table 7), has been neglected and assimilated to rock. The lack of geotechnical data  
402 could induce to questionable results when geological homogeneity of selected rock type profiles  
403 and the underlying bedrock under analyzed soil profiles is not assessed.

404 Three-component seismic signals recorded in directions North-South, East-West and Up-Down  
405 during the 9 Mw 11 March 2011 Tohoku earthquake (Table 8), at outcropping bedrock, are  
406 halved and propagated in the examined soil columns FKS011, IBR007 and MYG010.  
407 Acceleration signals are halved to take into account the free surface effect and integrated, to  
408 obtain the corresponding input data in terms of vertically incident velocities, before being forced  
409 at the base of the horizontal multilayer soil model, by the equation (3). The three components  
410 induce shear loading in horizontal directions  $x$  (NS) and  $y$  (EW) and pressure loading in  $z$ -  
411 direction (UD). Each signal recorded at rock sites has different amplitude and polarization. PGA  
412 and PGV can be referred to different directions of polarization (PGA and PGV are indicated by  
413 bold characters in Table 8).

414 Bedrock seismic records for NIGH11 (Table 8), provided by KiK-Net database (see Data and  
415 Resources Section), are measured at 205 m of depth. These borehole records, assumed as  
416 incident waves, are not halved before being forced at the base of the multilayer soil column.

417

#### 418 **Validation and discussion**

419 The validation of proposed model and numerical procedure is done by comparison of computed  
420 results with records in terms of surface time histories. Bedrock and surface time histories are  
421 compared to investigate amplification effects in alluvial deposits.

422 A preliminary study is done for soil profiles FKS011, IBR007 and MYG010, to identify the  
423 reference outcropping bedrock. In fact, a great variability of the computed surface response with  
424 the choice of the rock type profile, where the input signal is recorded, is noticed, especially in  
425 terms of amplitude. In Figures 3 and 4a, the various time histories of ground acceleration  
426 modulus at the surface are shown for the chosen rock type profiles associated to soil profile

427 FKS011. The rock type profile where the 3C seismic record, used as incident wave, provides the  
428 best numerical approximation of 3C surface record for the analyzed soil profile is identified as  
429 reference outcropping bedrock for that profile.

430 Acceleration moduli are compared in Figures 3(a, c, e) and 4a for soil profile FKS011, in  
431 Figures 5(a, c) and 6a for IBR007 and in Figure 7(a, c) for MYG010. The case referred as A/B is  
432 associated to soil profile A with incident signal deduced halving records in rock type profile B.  
433 The three acceleration components for the case of input signal recorded at the reference  
434 outcropping bedrock are shown, for soil profiles FKS011, IBR007 and MYG010, in Figure 8(a,  
435 b, c), respectively. Numerical results are consistent with recordings.

436 Obtained maximum accelerations are listed in Table 9 and their values are close to recorded  
437 acceleration peaks (Table 6). Bold values in Table 9 correspond to selected rock type profiles  
438 (reference outcropping bedrock), providing the best approximation of the acceleration modulus  
439 at the surface. Bold values in Table 10 are the computed maximum velocities best reproducing  
440 records. In soil profiles IBR007 and MYG010, the peak ground motion, both in terms of  
441 acceleration (Table 9) and velocity (Table 10), is better reproduced by input signals recorded in  
442 rock type profiles FKS031 and MYG011, respectively. The three-component signal recorded in  
443 rock type profile FKS015 allows a good approximation of the maximum components and  
444 modulus of acceleration in soil profile FKS011 (Table 9), while it is the signal recorded in rock  
445 type profile FKS031 that better reproduces the maximum components and modulus of velocity  
446 (Table 10).

447 The acceleration time history at the surface (Fig. 3(a, b)), produced by propagating the halved  
448 acceleration recorded in the rock type profile FKS004 along the soil column FKS011, is not a  
449 good approximation of the recorded signal. The too low average shear velocity of the rock type

450 profile FKS004, equal to 240 m/s (Table 7), could justify this inconsistency. It is important to  
451 notice the variability of seismic response at the surface of a soil column with characteristics of  
452 the selected rock type profile, identifying the outcropping bedrock considered in the theoretical  
453 model. The shear velocity profile with depth of assumed reference rock type columns and the  
454 distance between rock and soil profiles are parameters that could strongly influence the  
455 numerical seismic response in soil profiles. The bedrock to surface signal amplification is shown  
456 in Figures 3(b, d, f), 5(b, d) and 7(b, d) for soil profiles FKS011, IBR007 and MYG010,  
457 respectively. In soil profile MYG010, the acceleration signal amplification is no so significant  
458 compared with the reference bedrock signal (Fig. 7d), conversely to the other presented cases  
459 (Figs 4b and 7b).

460 Seismic response at the surface of soil profile NIGH11 is shown in Figure 9 in terms of  
461 maximum acceleration modulus. Numerical acceleration is slightly amplified compared with  
462 records. Further investigations could be undertaken by imposing a borehole boundary condition  
463 (instead of absorbing boundary condition (3)), at the soil-bedrock interface of the numerical  
464 model, to observe if this effect persist.

465 The assumption of soil density in NIGH11, not provided by KiK-Net database, could also  
466 influence the seismic site response.

467

#### 468 **1D-3C VS 1D-1C APPROACH**

469 The seismic response of a horizontally multilayered soil to the propagation of a three-component  
470 signal (1D-3C approach) is compared in the case of the 2011 Tohoku earthquake, to the  
471 superposition of the three independently propagated components (1D-1C approach). The shear  
472 modulus decreases, in the case of 1C propagation, according to the shear modulus decay curve

473 of the material obtained by laboratory tests. The stress-strain curve during a loading is referred  
474 to a backbone curve, obtained knowing the shear modulus decay curve.

475 Modeling the one-directional propagation of a three-component earthquake allows to take into  
476 account the interactions between shear and pressure components of the seismic load. Nonlinear  
477 and multiaxial coupling effects appear under a triaxial stress state induced by a cyclic 3D  
478 loading.

479 The comparison between 1D-1C and 1D-3C approaches is shown in Figure 10 for soil profiles  
480 FKS011 and IBR007, respectively, in terms of surface time histories. Stratigraphies and soil  
481 properties are given in Tables 2 and 3. The interaction between multiaxial stresses in the 3C  
482 approach yields a reduction of the ground motion at the surface. The modulus of acceleration at  
483 the outcropping bedrock appears amplified at the surface of analyzed soil columns for both 1D-  
484 1C and 1D-3C approaches, but peak accelerations are reduced in 1D-3C case and closer to  
485 records (Table 9). The PGV appears also reduced in the 1D-3C case, compared with the 1D-1C  
486 approach (Table 10).

487 The local response to a three-component earthquake in soil profiles FKS011 and IBR007 is  
488 analyzed in terms of depth profiles of maximum acceleration and velocity modulus and  
489 maximum octahedral stress and strain and in terms of stress-strain cycles in the most deformed  
490 layer (Figs 11 and 12).

491 The maximum motion modulus profile with depth shows, at each  $z$ -coordinate, the maximum  
492 modulus of the ground motion during shaking. The maximum acceleration modulus profiles with  
493 depth are displayed in these figures without low-pass filtering operations. Equation (13) is used  
494 to evaluate octahedral strains and stresses, which maximum values during the loading time are  
495 represented as profiles with depth. Hysteresis loops, at a given depth, are shown in terms of shear

496 strain and stress.

497 Maximum accelerations and velocities appear slightly higher for the combination of three 1C-  
498 propagations (1D-1C approach). Maximum stresses are reduced, in the 1D-3C case, and in softer  
499 layers maximum strains can be higher.

500 Cyclic shear strains with amplitude higher than the elastic behavior range limit give open loops  
501 in the shear stress-shear strain plane, exhibiting strong hysteresis. Due to nonlinear effects, the  
502 shear modulus decreases and the dissipation increases with increasing strain amplitude. The soil  
503 column cyclic responses in terms of shear stress and strain in  $x$ -direction when it is affected by a  
504 triaxial input signal (1D-3C) and when the  $x$ -component of the input signal is independently  
505 propagated (1D-1C) are compared in Figures 11(b, c) and 12(b, c). From one to three  
506 components, for a given maximum strain amplitude, the shear modulus decreases and the  
507 dissipation increases. Under triaxial loading the material strength is lower than for simple shear  
508 loading, referred to as the backbone curve.

509 Hysteresis loops for each horizontal direction are altered as a consequence of the interaction  
510 between loading components. This result confirms the findings of the parametric analysis using  
511 synthetic wavelets by Santisi d'Avila *et al.* (2012). In the case of one-component loading, the  
512 shape of the first loading curve is the same as the backbone curve and the shape of hysteresis  
513 loops remains unvaried at each cycle, for shear strains in the range of stable nonlinearity. In the  
514 case of three-component loading, the shape of the hysteresis loops changes at each cycle, also in  
515 a strain range that in the case of 1C loading is of stable nonlinearity, because the shape of loops  
516 is disturbed by the multiaxial stress coupling.

517 The main difference between 1D-1C and 1D-3C approach is remarkable in terms of ground  
518 motion time history, maximum stress and hysteretic behavior, with more nonlinearity and



519 coupling effects between components.

520

### 521 **1D-3C LOCAL SEISMIC RESPONSE ANALYSIS IN THE TOHOKU AREA**

522 This research aims to provide a tool to study the local seismic response in case of strong  
523 earthquakes affecting alluvial sites. The proposed model allows to preview possible  
524 amplifications of seismic motion at the surface, influenced by stratigraphic characteristics, and to  
525 evaluate non-measured parameters of motion, stress and strain along the soil profiles, in order to  
526 investigate nonlinear effects in deeper detail. Depth profiles of maximum acceleration and  
527 velocity modulus, maximum octahedral stress and strain are shown in Figures 11a, 12a and 13a,  
528 for soil profiles FKS011, IBR007, MYG010, respectively. The results for soil profile NIGH11  
529 are shown in Figure 14.

530 Soft layers and high strain drops at layer interfaces can be identified evaluating the maximum  
531 strain profiles with depth. We observe that maximum strains along the soil profile are present in  
532 layer interfaces (Figs 11a, 12a, 13a and 14).

533 The 1D-3C approach allows to evaluate non-measured parameters of motion, stress and strain  
534 along the analyzed soil profile, influenced by the input motion polarization and 3D loading path.  
535 Non null strain and stress components are assessed along the soil profile, namely the three strains  
536 in  $z$ -direction,  $\gamma_{yz}$ ,  $\gamma_{yz}$  and  $\epsilon_{zz}$ , and consequent stresses  $\sigma_{xx}$ ,  $\sigma_{yy}$ ,  $\tau_{yz}$ ,  $\tau_{zx}$  and  $\sigma_{zz}$ .

537 The shape of the shear stress-strain cycles in  $x$ -direction (respectively  $y$ -direction) reflects  
538 coupling effects with loads in directions  $y$  (respectively  $x$ ) and  $z$ . At a given depth, nonlinear  
539 effects are more important for the minimum peak horizontal component that is the most  
540 influenced by three-dimensional motion coupling (Figs 11c, 12c and 13b).

541 In particular for the Tohoku earthquake, we detect, in all hysteresis loops (Figs 11(b, c), 12(b, c))

542 and 13(b, c)), two successive events (Bonilla *et al.*, 2011). This earthquake feature is also  
543 observed in a time-frequency polarization analysis. Stockwell amplitude spectra of separate  
544 horizontal acceleration components at the surface are compared in Figure 15, for records (up)  
545 and numerical computations (down) in  $x$ - (Fig. 15a) and  $y$ -direction (Fig. 15b). Two successive  
546 events can be easily distinguished, the range of frequencies involved throughout the time is  
547 coherent and spectral amplitudes are similar for given time and frequency. That confirms the  
548 reliability of the proposed model. It will be interesting to investigate, in a future study, the  
549 different response of a soil column to two independent and successive events.

550 In Figure 13b, we can remark a completely negligible overtaking of the one-dimensional soil  
551 strength (backbone curve). This numerical error of the three-dimensional soil behavior routine,  
552 due to convergence difficulties, becomes more evident for strains higher than about 5 %, when  
553 the constitutive model gets to be unusable (Lenti, 2006). The implemented M<sub>PII</sub> type model  
554 gives reliable results in a range of stable nonlinearity. Liquefaction problems cannot be  
555 investigated. Being the proposed propagation model totally independent of the applied  
556 constitutive relation, a major goal is to implement a relation for saturated soils.

557 The variability of seismic response at the surface of soil columns with the characteristics of  
558 selected rock type profiles, approximating the outcropping bedrock, demands future statistical  
559 studies to analyze the local seismic response of a site accounting for various rock profiles and  
560 different earthquake records.

561

## 562 **CONCLUSIONS**

563 A one-dimensional three-component geomechanical model is proposed and discussed, to analyze  
564 the propagation of 3C seismic waves due to the strong quakes in 1D soil profiles (1D-3C

565 approach). A promising solution for strong seismic motion evaluation and site effect analysis is  
566 provided.

567 A three-dimensional constitutive relation of the Masing-Prandtl-Ishlinskii-Iwan (MPII) type, for  
568 cyclic loading, is implemented in a finite element scheme, modeling a horizontally layered soil.

569 The adopted rheological model for soils has been selected for its 3D features with nonlinear  
570 behavior for both loading and unloading and, above all, because few parameters are necessary to  
571 characterize the soil hysteretic behavior.

572 The analysis of four soil profiles in the Tohoku area (Japan), shaken by the 9 Mw 11 March 2011  
573 Tohoku earthquake, is presented in this paper. The validation of the 1D-3C approach against  
574 recorded surface time histories is carried out and the reliability of the proposed model is  
575 confirmed.

576 We selected, in this study, some rock type profiles close to analyzed soil profiles and we use as  
577 incident loading the halved signal recorded at rock outcrops. The variability of the surface  
578 ground motion with the bedrock incident loading is observed. The signal recorded in outcropping  
579 bedrock, permitting to obtain the best approximation of the surface seismic record is assumed as  
580 reference bedrock motion for the analyzed soil profile. The lack of geotechnical data could  
581 induce to questionable results when geological homogeneity of selected rock type outcrops and  
582 the modeled bedrock underlying analyzed multilayered soils is not assessed. More quantitative  
583 analyses could be undertaken when more available input data will permit to increase the  
584 accuracy of results. Statistical studies using records of different earthquakes at a same site could  
585 be undertaken using the 1D-3C approach for the evaluation of local seismic response for site  
586 effect analyses.

587 The combination of three separate 1D-1C nonlinear analyses is compared to the proposed 1D-3C

588 approach. Motion amplification effects at the surface are reduced in the 1D-3C approach due to  
589 nonlinearities and three-dimensional motion coupling. Multiaxial stress states induce strength  
590 reduction of the material and larger damping effects. The shape of hysteresis loops changes at  
591 each cycle in the 1D-3C approach, also in a strain range that in the case of one-component  
592 loading is of stable nonlinearity.

593 Effects of the input motion polarization and 3D loading path can be detected by the 1D-3C  
594 approach, that allow to evaluate non-measured parameters of motion, stress and strain along the  
595 analyzed soil profile, in order to detail nonlinear effects. Soil properties such as the Poisson's  
596 ratio have great impact on local seismic response, influencing the soil dissipative properties.  
597 Input motion properties such as the polarization (vertical to horizontal component ratio) affect  
598 energy dissipation rate and the amplification effect. In particular, a low seismic velocity ratio in  
599 the soil and a high vertical to horizontal component ratio increase the three-dimensional  
600 mechanical interaction and progressively change the hysteresis loop size and shape at each cycle.  
601 Maximum strains are induced in layer interfaces, where waves encounter large variations of  
602 impedance contrast, along the soil profile. Nonlinearity effects are more important in the  
603 direction of minimum peak horizontal component that is the most influenced by three-  
604 dimensional motion coupling.

605 In particular for the 2011 Tohoku earthquake, the two successive events, detected by records, are  
606 numerically reproduced (hysteresis loops, Stockwell amplitude spectra).

607 The extension of the proposed 1D-3C approach to higher strain rates is planned as further  
608 investigation to be able to study the effects of soil nonlinearity in saturated conditions.

609

610

611 **DATA AND RESOURCES**

612 Seismograms and soil stratigraphic setting used in this study are provided by the National  
613 research Institute for Earth science and Disaster prevention (NIED), in Japan, and can be  
614 obtained from the Kyoshin and Kiban-Kyoshin Networks at [www.k-net.bosai.go.jp](http://www.k-net.bosai.go.jp) (last  
615 accessed May 2012).

616

617 **ACKNOWLEDGMENTS**

618 We are grateful to Florent De Martin as well as an anonymous reviewer, for their careful  
619 revision of this manuscript and their constructive suggestions.

620

621 **REFERENCES**

622 Bardet, J. P., K. Ichii, and C. H. Lin (2000). *EERA: A computer program for Equivalent-linear*  
623 *Earthquake site Response Analyses of layered soil deposits*, University of Southern California,  
624 United States.

625 Bardet, J. P., and T. Tobita (2001). *NERA: A computer program for Nonlinear Earthquake site*  
626 *Response Analyses of layered soil deposits*, University of Southern California, United States.

627 Bertotti, G., and I. Mayergoyz (2006). *The science of hysteresis: mathematical modeling and*  
628 *applications*, Elsevier, Amsterdam, Netherlands.

629 Bonilla, L. F., J. H. Steidl, J. C. Gariel, and R. J. Archuleta (2002). Borehole response studies at  
630 the Garner Valley downhole array, Southern California, *Bull. Seism. Soc. Am.*, **92**, 3165–3179.

631 Bonilla, L. F., K. Tsuda, N. Pulido, J. Régnier, and A. Laurendeau (2011). Nonlinear site  
632 response evidence of K-Net and KiK-Net records from the 2011 off the Pacific coast of Tohoku  
633 Earthquake, *Earth Planets Space*, **63**, 785–789.

634 Crisfield, M. A. (1991). *Non-linear finite element analysis of solids and structures*, vol. 1, John  
635 Wiley and Sons, Chichesrter, England.

636 Fahey, M. (1992). Shear modulus of cohesionless soil: variation with stress and strain level,  
637 *Can. Geotech. J.*, **29**, 157–161.

638 Fung, Y. C. (1965). *Foundation of soil mechanics*, Prentice Hall, Englewood Cliffs, New Jersey.

639 Hardin, B. O., and V. P. Drnevich (1972a). Shear modulus and damping in soil: measurement  
640 and parameter effects, *J. Soil Mech. Found. Div.*, **98**, 603–624.

641 Hardin, B. O., and V. P. Drnevich (1972b). Shear modulus and damping in soil: design  
642 equations and curves, *J. Soil Mech. Found. Div.*, **98**, 667–692.

643 Hilber, H. M., T. J. R. Hughes, and R. L. Taylor (1977). Improved numerical dissipation for  
644 time integration algorithms in structural dynamics, *Earthquake Eng. Struct. Dyn.*, **5**, 283–292.

645 Hughes, T. J. R. (1987). *The finite element method - Linear static and dynamic finite element*  
646 *analysis*, Prentice Hall, Englewood Cliffs, New Jersey.

647 Hsu, C. C., and M. Vucetic (2004). Volumetric threshold shear strain for cyclic settlement, *J.*  
648 *Geotech. Geoenviron. Eng.*, **130**(1), 58–70.

649 Hsu, C. C., and M. Vucetic (2006). Threshold shear strain for cyclic pore-water pressure in  
650 cohesive soils, *J. Geotech. Geoenviron. Eng.*, **132**(10), 1325–1335.

651 Ishihara, K. (1996). *Soil behaviour in earthquake geotechnics*, Clarenton Press, Oxford,  
652 England.

653 Iwan, W. D. (1967). On a class of models for the yielding behavior of continuous and composite  
654 systems, *J. Appl. Mech.*, **34**, 612–617.

655 Joyner, W. (1975). A method for calculating nonlinear seismic response in two dimensions,  
656 *Bull. Seism. Soc. Am.*, **65**(5), 1337–1357.

657 Joyner, W. B., and A. T. F. Chen (1975). Calculation of nonlinear ground response in  
658 earthquakes, *Bull. Seism. Soc. Am.*, **65**(5), 1315–1336.

659 Kim, T. C., and M. Novak (1981). Dynamic properties of some cohesive soils of Ontario, *Can.*  
660 *Geotech. J.*, **18**, 371–389.

661 Kramer, S. L. (1996). *Geotechnical earthquake engineering*, Prentice Hall, New Jersey.

662 Kuhlemeyer, R. L., and J. Lysmer (1973). Finite element method accuracy for wave propagation  
663 problems, *J. Soil Mech. Found. Div.*, **99**(SM5), 421–427.

664 Lee, K. W., and W. D. L. Finn (1978). DESRA-2: Dynamic effective stress response analysis of  
665 soil deposits with energy transmitting boundary including assessment of liquefaction potential,  
666 in *Soil Mechanics Series*, University of British Columbia, Vancouver.

667 Lefebvre, G. S., Leboeuf D., and B. Demers (1989). Stability threshold for cyclic loading of  
668 saturated clay, *Can. Geotech. J.*, **26**, 122–131.

669 Lenti, L. (2006). *Modellazione di effetti non lineari in terreni soggetti a carico ciclico e*  
670 *dinamico (Modeling of nonlinear effects in soils for cyclic and dynamic loading)*, PhD thesis,  
671 Università di Bologna Alma Mater Studiorum.

672 Li, X. S. (1990). *Free field response under multidirectional earthquake loading*, PhD thesis,  
673 University of California, Davis.

674 Li, X. S., Z. L. Wang, and C. K. Shen (1992). *SUMDES: A nonlinear procedure for response*  
675 *analysis of horizontally-layered sites subjected to multi-directional earthquake loading*,  
676 University of California, Davis.

677 Newmark, N. M. (1959). A method of computation for structural dynamics. *J. Eng. Mech.*,  
678 **85**(EM3), 67–94.

679 Oppenheim, A. V., A. S. Willsky, and S. H. Nawab (1997). *Signals and systems*, 2nd edn,  
680 Prentice Hall.

681 Santisi d’Avila M. P., L. Lenti, and J. F. Semblat (2012). Modeling strong seismic ground  
682 motion: 3D loading path vs wavefield polarization, *Geophys. J. Int.*, **190**, 1607–1624.

683 Satoh, T., H. Kawase, and T. Sato (1995). Evaluation of local site effects and their removal from  
684 borehole records observed in the Sendai region, Japan, *Bull. Seism. Soc. Am.*, **85**, 1770–1789.

685 Schnabel, P. B., J. Lysmer, and H. B. Seed (1972). SHAKE: A computer program for  
686 earthquake response analysis of horizontally layered sites, *Report UCB/EERC-72/12*,  
687 Earthquake Engineering Research Center, University of California, Berkeley, United States.

688 Seed, H. B., and I. M. Idriss (1970a). Soil moduli and damping factors for dynamic response  
689 analyses, *Report UCB/EERC-70/10*, Earthquake Engineering Research Center, University of  
690 California, Berkeley.

691 Seed, H. B., and I. M. Idriss (1970b). Analyses of ground motions at Union Bay, Seattle, during  
692 earthquakes and distant nuclear blasts, *Bull. Seism. Soc. Am.*, **60**, 125–136.

693 De Martin, F., H. Kawase, and A. Modaressi (2010). Nonlinear soil response of a borehole  
694 station based on one-dimensional inversion during the 2005 West off Fukuoka Prefecture  
695 earthquake, *Bull. Seism. Soc. Am.*, **100**, 151–171.

696 Seed, H. B., and J. I. Sun (1989). Implication of site effects in the Mexico City earthquake of  
697 September 19, 1985 for Earthquake-Resistant Design Criteria in the San Francisco Bay Area of  
698 California, *Report UCB/EERC-89/03*, Earthquake Engineering Research Center, University of



699 California, Berkeley.

700 Seed H. B., R. T. Wong, I. M. Idriss, and K. Tokimatsu (1986). Moduli and damping factors for  
701 dynamic analyses of cohesionless soils, *Report UCB/EERC-84/14*, Earthquake Engineering  
702 Research Center, University of California, Berkeley.

703 Segalman, D. J., and M. J. Starr (2008). Inversion of Masing models via continuous Iwan  
704 systems, *Int. J. Nonlinear Mech.*, **43**, 74–80.

705 Semblat, J. F., and J. J. Brioist (2000). Efficiency of higher order finite elements for the analysis  
706 of seismic wave propagation, *J. Sound Vibrat.*, **231**(2), 460–467.

707 Sun, J. I., R. Golesorkhi, and H. B. Seed (1988). Dynamic moduli and damping ratios for  
708 cohesive soils, *Report UCB/EERC-88/15*, Earthquake Engineering Research Center, University  
709 of California, Berkeley.

710 Vucetic, M., and R. Dobry (1991). Effect of soil plasticity on cyclic response, *J. Geotech. Eng.*,  
711 **117**(1), 89–107.

712 Vucetic, M. (1994). Cyclic threshold shear strains in soils, *J. Geotech. Eng.*, **120**(12), 2208–  
713 2228.

714 Wang, Z. L., Y. F. Dafalias, and C. K. Shen (1990). Bounding surface hypoelasticity model for  
715 sand, *J. Eng. Mech.*, **116**(5), 983–1001.

716 Zambelli, C., C. Di Prisco, A. D'Onofrio, C. Visone, and F. Santucci de Magistris (2006).  
717 Dependency of the mechanical behavior of granular soils on loading frequency: experimental  
718 results and constitutive modelling, in *Soil Stress-Strain Behavior: Measurement, Modeling and*  
719 *Analysis, A collection of papers of the Geotechnical Symposium in Roma, March 16- 17, 2006*,  
720 567–582.

721 **AUTHORS' AFFILIATION**

722 Maria Paola Santisi d'Avila

723 Laboratoire Jean Alexandre Dieudonné

724 University of Nice Sophia Antipolis

725 Parc Valrose

726 Nice, France 06108

727

728 Jean-François Semblat and Luca Lenti

729 IFSTTAR

730 University Paris-Est

731 14 Boulevard Newton

732 Marne la Vallée, France 77447

733

734

735

736

737

738

739

740

741

742

743

744 **TABLES**

745

746 **Table 1.** Selected soil profiles in Tohoku area (Japan)

Site name - Prefecture	Site code	Epicentral distance (km)	Depth H (m)	Average $v_s$ (m/s)	$\min \{v_p / v_s\}$
IWAKY - FUKUSHIMAKEN	FKS011	206	10.00	222	3.05
NAKAMINATO - IBARAKIKEN	IBR007	279	20.35	239	2.30
ISHINOMAKI - MIYAGIKEN	MYG010	143	20.45	247	4.62
KAWANISHI - NIIGATAKEN	NIGH11	378	205.0	578	2.45

747

748

749 **Table 2.** Stratigraphy and soil properties of profile FKS011

FKS011	H-z (m)	th (m)	$\rho$ (kg/m <sup>3</sup> )	$v_s$ (m/s)	$v_p$ (m/s)	$\gamma_r$ (‰)
Fill soil	2.2	2.2	1430	100	700	0.800
	3	0.8	1650	210	700	0.427
Silt	4	1	1720	210	1300	0.427
	5.95	1.95	1660	330	1300	0.427
Clay	6.85	0.9	1810	330	1300	2.431
	8	1.15	1970	330	1300	100
Rock	9	1	1980	590	1800	100
	10	1	2060	590	1800	100

750

751

752 **Table 3.** Stratigraphy and soil properties of profile IBR007

IBR007	H-z (m)	th (m)	$\rho$ (kg/m <sup>3</sup> )	$v_s$ (m/s)	$v_p$ (m/s)	$\gamma_r$ (‰)
Fill soil	2	2	1450	80	260	1.065
	3.9	1.9	1750	150	520	1.065
Volcanic ash clay	4.4	0.5	1810	150	520	1.065
Sand	6	1.6	1910	200	1220	0.368
	7.8	1.8	1850	200	1220	0.368
Silt	9	1.2	1770	200	1220	0.427
	10	1	1810	530	1220	0.427
	11.2	1.2	1920	530	1220	0.427
Sand	12.7	1.5	1980	530	1220	0.368
Gravel	14.1	1.4	2060	530	1220	0.143
Clay	15.1	1	1880	530	1220	2.431
Sand	16	0.9	1960	610	1920	0.368
	17	1	1880	610	1920	0.368
	20.35	3.35	1900	610	1920	0.368

753

754

755 **Table 4.** Stratigraphy and soil properties of profile MYG010

MYG010	H-z (m)	th (m)	$\rho$ (kg/m <sup>3</sup> )	$v_s$ (m/s)	$v_p$ (m/s)	$\gamma_r$ (‰)
Fill soil	1.5	1.5	1600	100	280	0.368
Sand	2	0.5	1660	150	1480	0.368
	3	1	1810	150	1480	0.368
	4	1	1950	150	1480	0.368
	5	1	1900	320	1480	0.368
	6	1	1860	320	1480	0.368
	7	1	1900	320	1480	0.368
	8	1	1810	320	1480	0.368
	17	9	1890	300	1480	0.368
	20.45	3.45	1850	300	1480	0.368

756

757

758 **Table 5.** Stratigraphy and soil properties of profile NIGH11

NIGH11	H-z (m)	th (m)	$\rho$ (kg/m <sup>3</sup> )	$v_s$ (m/s)	$v_p$ (m/s)	$\gamma_r$ (‰)
Fill soil	2	2	1800	200	500	0.143
Gravel	30	28	1800	400	1830	0.143
Rock	46	16	1900	400	1830	100
Silt	57	11	1900	400	1830	0.427
	63	6	1900	700	1830	100
Rock	85	22	1900	520	1830	100
	185	100	1900	650	1830	100
Gravel	198	13	1800	850	2080	0.143
Rock	205	7	2000	850	2080	100

759

760

761 **Table 6.** Acceleration and velocity recorded at the surface of selected soil profiles during the

762 2011 Tohoku earthquake

Site code	$a_x$ (m/s <sup>2</sup> )	$a_y$ (m/s <sup>2</sup> )	$a_z$ (m/s <sup>2</sup> )	$ a $ (m/s <sup>2</sup> )	$a_z / \max \{a_x, a_y\}$ (%)	$v_x$ (m/s)	$v_y$ (m/s)	$v_z$ (m/s)	$ v $ (m/s)	$v_z / \max \{v_x, v_y\}$ (%)
FKS011	<b>3.74</b>	3.12	3.00	<b>4.47</b>	80	<b>0.39</b>	0.34	0.12	<b>0.47</b>	31
IBR007	<b>5.43</b>	5.10	4.12	<b>5.87</b>	76	0.29	<b>0.44</b>	0.13	<b>0.49</b>	30
MYG010	<b>4.58</b>	3.77	3.32	<b>4.88</b>	72	0.50	<b>0.56</b>	0.16	<b>0.68</b>	29
NIGH11	<b>0.22</b>	0.18	0.16	<b>0.26</b>	73	0.050	<b>0.056</b>	0.041	<b>0.058</b>	73

763

764

765 **Table 7.** Selected rock type profiles in Tohoku area (Japan)

Site name	Prefecture	Site code	Epicentral distance (km)	Depth H (m)	Average $v_s$ (m/s)	Surface soil depth (m)
IITATE	FUKUSHIMAKEN	FKS004	193	10.42	240	0.50
TANAGURA	FUKUSHIMAKEN	FKS015	250	10.03	463	0.50
NIHOMMATSU	FUKUSHIMAKEN	FKS019	220	11.27	1025	0.20
KAWAUCHI	FUKUSHIMAKEN	FKS031	199	10.11	437	-
OHFUNATO	IWATEKEN	IWT008	148	10.00	750	0.15
OSHIKA	MIYAGIKEN	MYG011	121	20.00	1220	0.05
UTSUNOMIYA	TOCHIGIKEN	TCG007	314	10.14	388	2.30

766

767

768 **Table 8.** Acceleration and velocity recorded at the surface of selected rock type profiles and

769 borehole acceleration and velocity recorded in soil profile NIGH11, during the 2011 Tohoku

770 earthquake

Site code	$a_x$ (m/s <sup>2</sup> )	$a_y$ (m/s <sup>2</sup> )	$a_z$ (m/s <sup>2</sup> )	$ a $ (m/s <sup>2</sup> )	$a_z / \max \{a_x, a_y\}$ (%)	$v_x$ (m/s)	$v_y$ (m/s)	$v_z$ (m/s)	$ v $ (m/s)	$v_z / \max \{v_x, v_y\}$ (%)
FKS004	<b>2.98</b>	2.53	1.49	3.53	50	<b>0.21</b>	0.17	0.08	0.23	38
FKS015	<b>1.36</b>	1.01	0.58	1.42	43	<b>0.17</b>	0.16	0.10	0.18	59
FKS019	2.07	<b>2.16</b>	0.84	2.29	39	0.27	<b>0.30</b>	0.13	0.30	44
FKS031	<b>2.34</b>	2.17	1.43	2.40	61	<b>0.34</b>	0.29	0.12	0.37	35
IWT008	1.26	<b>1.66</b>	0.61	2.03	37	0.10	<b>0.14</b>	0.09	0.17	64
MYG011	<b>4.39</b>	3.26	1.24	4.42	28	0.19	<b>0.37</b>	0.16	0.38	43
TCG007	0.81	<b>0.86</b>	0.60	0.98	70	0.19	<b>0.14</b>	0.09	0.19	47
NIGH11	<b>0.14</b>	0.14	0.13	0.15	96	0.042	<b>0.058</b>	0.039	0.059	67

771

772

773 **Table 9.** Numerical acceleration evaluated at the surface of selected soil profiles

Soil profile site code	Rock profile site code	$a_x$ (m/s <sup>2</sup> )	$a_y$ (m/s <sup>2</sup> )	$a_z$ (m/s <sup>2</sup> )	a  (m/s <sup>2</sup> )	
					1D-3C	1D-1C
FKS011	FKS004	5.99	5.50	2.94	5.68	
FKS011	<b>FKS015</b>	3.78	3.92	1.64	<b>4.55</b>	5.72
FKS011	FKS019	4.66	5.06	1.68	4.76	
FKS011	FKS031	4.97	4.50	2.78	4.99	
IBR007	FKS015	3.73	3.21	2.21	3.95	
IBR007	<b>FKS031</b>	5.59	5.45	2.73	<b>6.07</b>	7.54
IBR007	TCG007	3.04	3.05	2.09	3.45	
MYG010	IWT008	3.11	2.91	3.11	3.23	
MYG010	<b>MYG011</b>	4.08	3.75	3.43	<b>4.85</b>	
NIGH11	<b>NIGH11</b>	0.33	0.38	0.28	<b>0.39</b>	

774

775

776 **Table 10.** Numerical velocity evaluated at the surface of selected soil profiles

Soil profile site code	Rock profile site code	$v_x$ (m/s)	$v_y$ (m/s)	$v_z$ (m/s)	v  (m/s)	
					1D-3C	1D-1C
FKS011	FKS004	0.32	0.25	0.08	0.33	
	<b>FKS015</b>	0.25	0.23	0.10	0.25	0.26
	FKS019	0.37	0.42	0.13	0.43	
	<b>FKS031</b>	<b>0.43</b>	<b>0.38</b>	<b>0.12</b>	<b>0.48</b>	
IBR007	FKS015	0.21	0.25	0.11	0.28	
	<b>FKS031</b>	<b>0.39</b>	<b>0.38</b>	<b>0.15</b>	<b>0.48</b>	0.52
	TCG007	0.26	0.18	0.10	0.26	
MYG010	IWT008	0.16	0.20	0.09	0.24	
	<b>MYG011</b>	<b>0.17</b>	<b>0.42</b>	<b>0.16</b>	<b>0.45</b>	
NIGH11	<b>NIGH11</b>	0.11	0.15	0.08	0.15	

777

778

779 **FIGURE CAPTIONS**

780 **Figure 1.** Spatial discretization of a horizontally layered soil forced at its base by a halved three-  
781 component earthquake, recorded at a close outcropping bedrock site.

782 **Figure 2.** Geographical position of analyzed K-Net stations, placed at the surface of soil (**bold**)  
783 and rock type (*italic*) profiles, in the Tohoku area (Japan).

784 **Figure 3.** Time history of acceleration modulus during Tohoku earthquake: measured data and  
785 numerical solution at the ground surface (a, c, e); reference bedrock signal and surface numerical  
786 solution (b, d, f), for cases FKS011/FKS004 (a,b), FKS011/FKS019 (c,d) and FKS011/FKS031  
787 (e, f).

788 **Figure 4.** Time history of acceleration modulus during Tohoku earthquake: measured data and  
789 numerical solution at the ground surface (a); reference bedrock signal and surface numerical  
790 solution (b), for case FKS011/FKS015.

791 **Figure 5.** Time history of acceleration modulus during Tohoku earthquake: measured data and  
792 numerical solution at the ground surface (a, c); reference bedrock signal and surface numerical  
793 solution (b, d), for cases IBR007/FKS015 (a,b) and IBR007/TCG007 (c,d).

794 **Figure 6.** Time history of acceleration modulus during Tohoku earthquake: measured data and  
795 numerical solution at the ground surface (a); reference bedrock signal and surface numerical  
796 solution (b), for case IBR007/FKS031.

797 **Figure 7.** Time history of acceleration modulus during Tohoku earthquake: measured data and  
798 numerical solution at the ground surface (a, c); reference bedrock signal and surface numerical  
799 solution (b, d), for cases MYG010/IWT008 (a,b) and MYG010/MYG011 (c,d).

800 **Figure 8.** Three-component acceleration time history at the ground surface during Tohoku



801 earthquake: measured data and numerical solution in directions x (left), y (middle) and z (right),  
802 for cases FKS011/FKS015 (a), IBR007/FKS031 (b) and MYG010/MYG011 (c).

803 **Figure 9.** Time history of acceleration modulus during Tohoku earthquake: measured data and  
804 numerical solution at the ground surface (a); reference bedrock signal and surface numerical  
805 solution (b), for soil profile NIGH11.

806 **Figure 10.** Time history of acceleration modulus at the ground surface during Tohoku  
807 earthquake: 1D-3C and 1D-1C numerical solutions for cases FKS011/FKS015 (a) and  
808 IBR007/FKS031 (b).

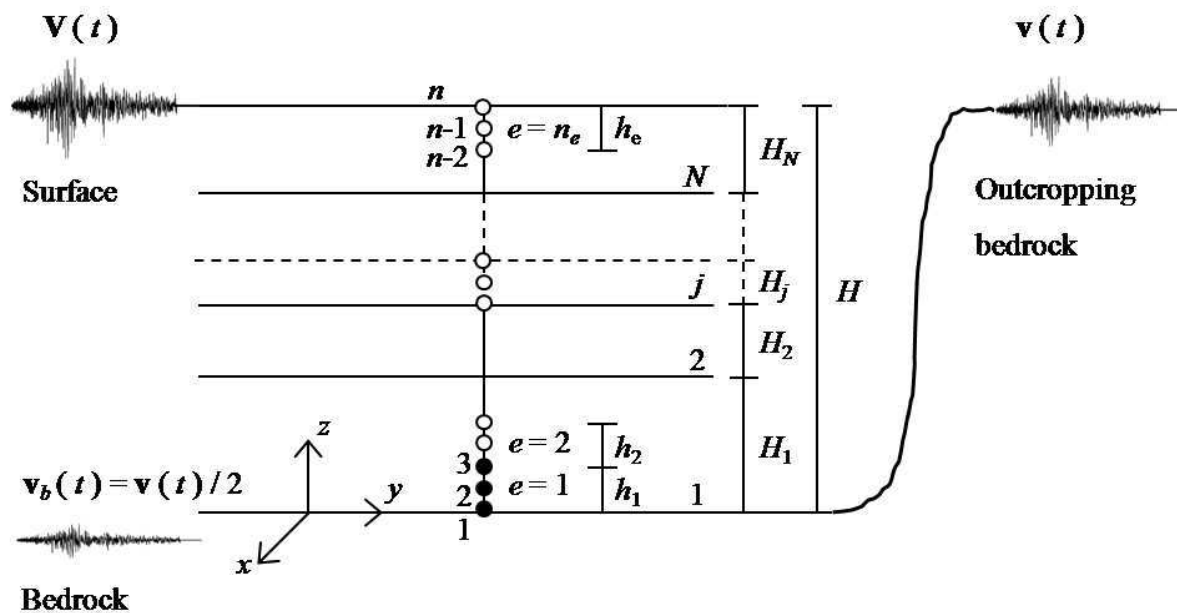
809 **Figure 11.** 1D-3C and 1D-1C seismic response during the Tohoku earthquake, for the case  
810 FKS011/FKS015: profiles of maximum acceleration and velocity modulus, octahedral strain and  
811 stress with depth (a); shear stress-strain loops at 2 m depth in x- (b) and y-direction (c).

812 **Figure 12.** 1D-3C and 1D-1C seismic response during the Tohoku earthquake, for the case  
813 IBR007/FKS031: profiles of maximum acceleration and velocity modulus, octahedral strain and  
814 stress with depth (a); shear stress-strain loops at 8.5 m depth in x- (b) and y-direction (c).

815 **Figure 13.** 1D-3C and 1D-1C seismic response during the Tohoku earthquake, for the case  
816 MYG010/MYG011: profiles of maximum acceleration and velocity modulus, octahedral strain  
817 and stress with depth (a); shear stress-strain loops at 3.5 m depth in x- (b) and y-direction (c).

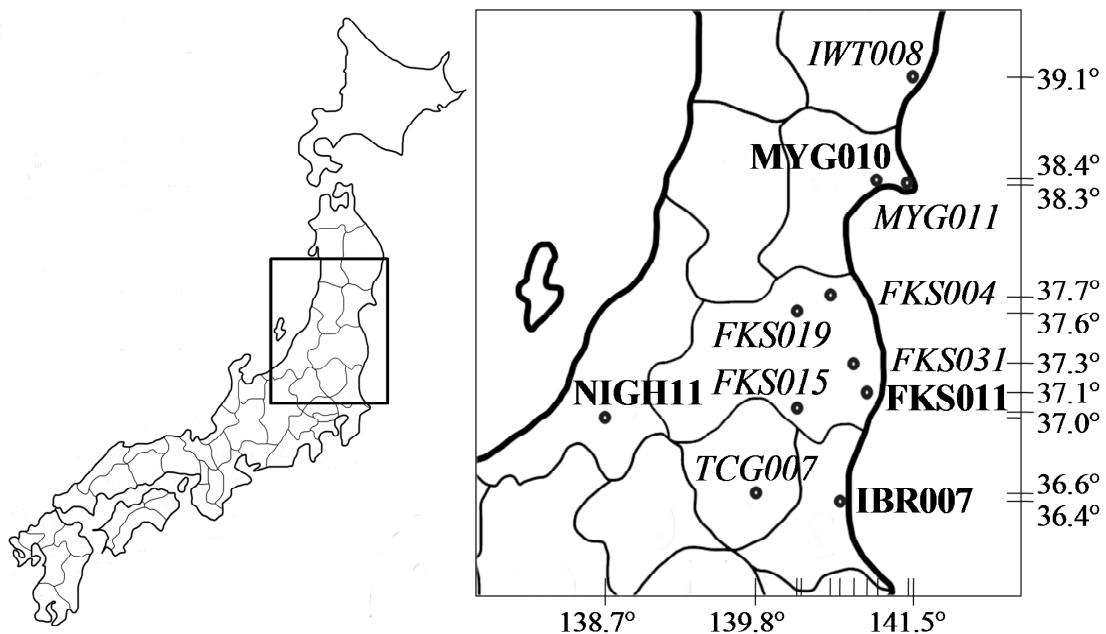
818 **Figure 14.** Maximum acceleration, velocity, octahedral strain and stress profiles with depth in  
819 soil profile NIGH11 during 2011 Tohoku earthquake.

820 **Figure 15.** Spectral amplitude variation with time and frequency at the ground surface, in  
821 horizontal directions x (a) and y (b), during the Tohoku earthquake, evaluated using measured  
822 acceleration (up) and computed acceleration (down) as input, for the case MYG010/MYG011.

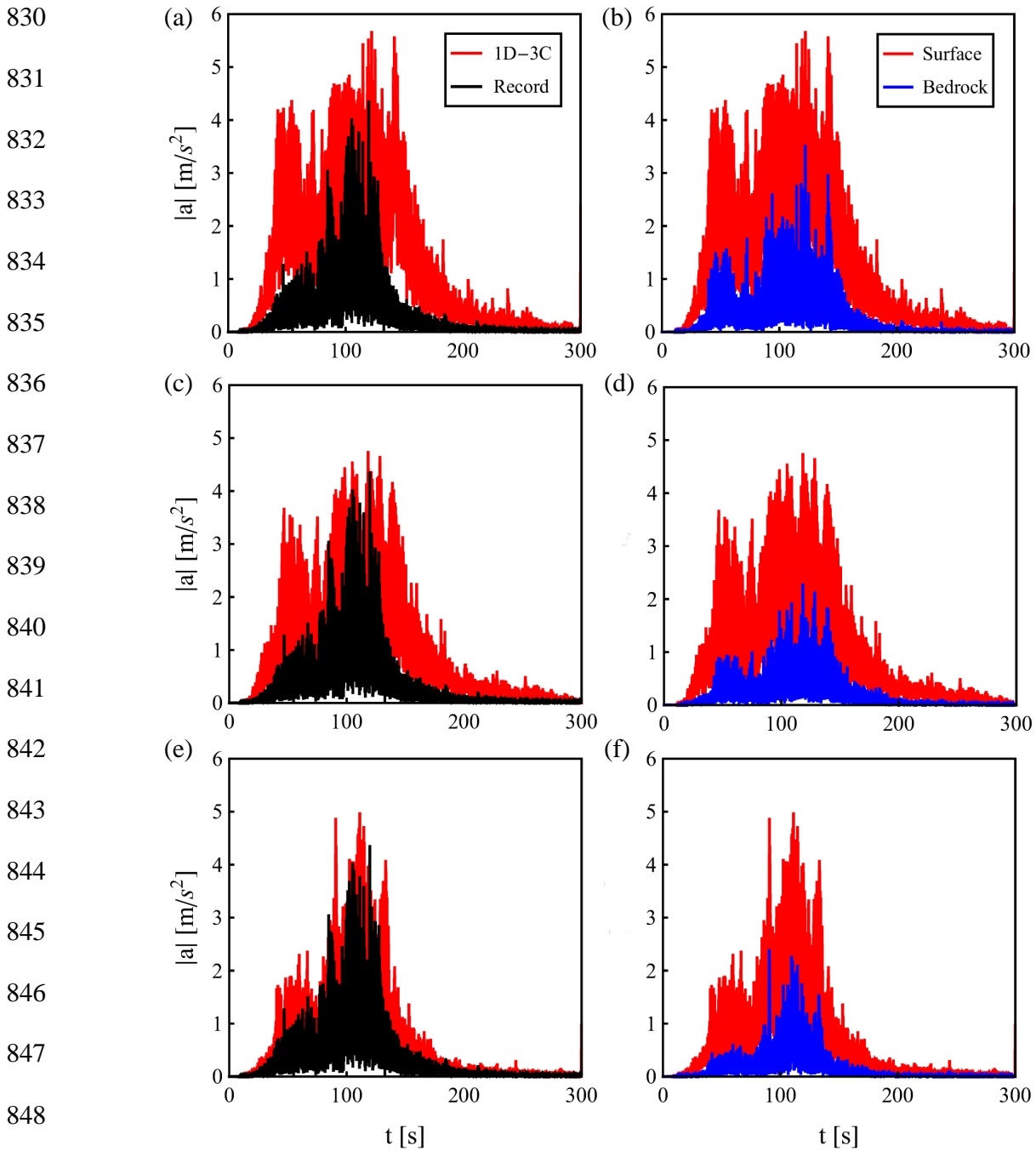


823  
 824 **Figure 1.** Spatial discretization of a horizontally layered soil forced at its base by a halved three-  
 825 component earthquake, recorded at a close outcropping bedrock site.

826



827  
 828 **Figure 2.** Geographical position of analyzed K-Net stations, placed at the surface of soil (**bold**)  
 829 and rock type (*italic*) profiles, in the Tohoku area (Japan).

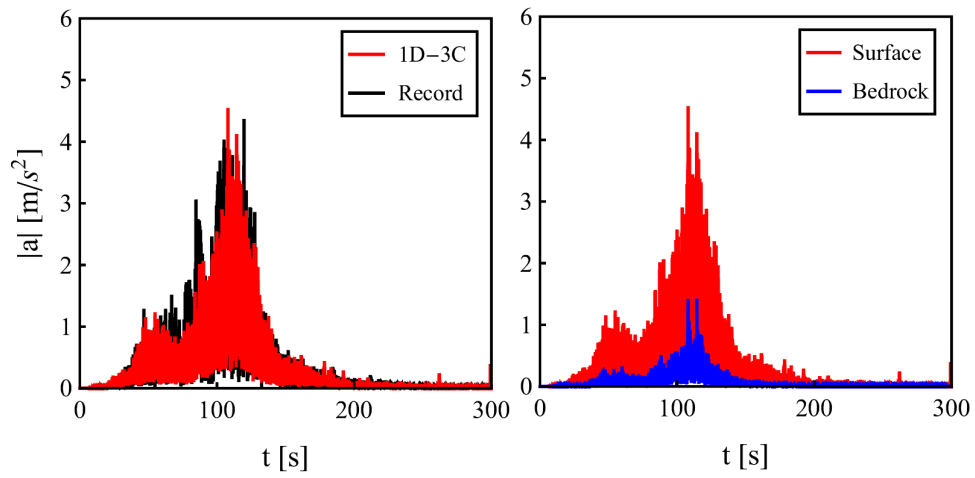


849 **Figure 3.** Time history of acceleration modulus during Tohoku earthquake: measured data and  
 850 numerical solution at the ground surface (a, c, e); reference bedrock signal and surface numerical  
 851 solution (b, d, f), for cases FKS011/FKS004 (a,b), FKS011/FKS019 (c,d) and FKS011/FKS031  
 852 (e, f).

853

(a)

(b)



854

855 **Figure 4.** Time history of acceleration modulus during Tohoku earthquake: measured data and  
856 numerical solution at the ground surface (a); reference bedrock signal and surface numerical  
857 solution (b), for case FKS011/FKS015.

858

859

860

861

862

863

864

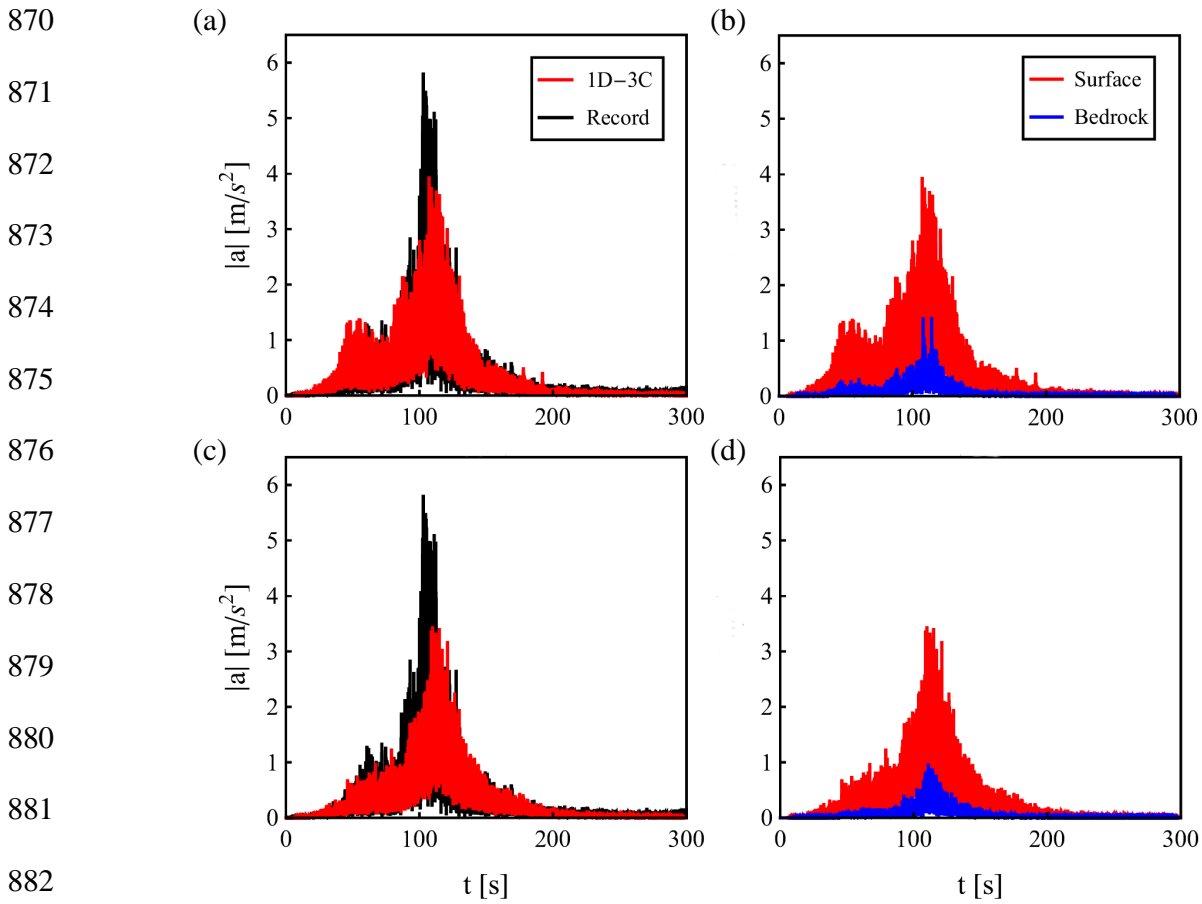
865

866

867

868

869



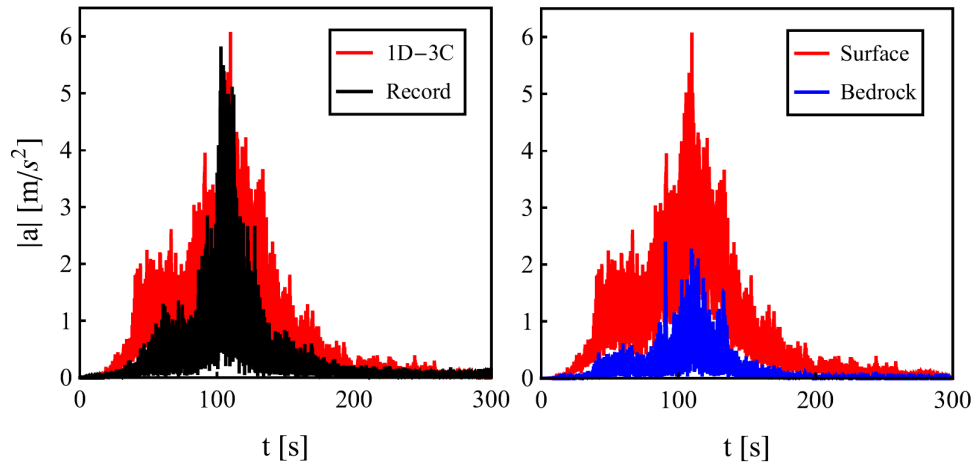
883 **Figure 5.** Time history of acceleration modulus during Tohoku earthquake: measured data and  
 884 numerical solution at the ground surface (a, c); reference bedrock signal and surface numerical  
 885 solution (b, d), for cases IBR007/FKS015 (a,b) and IBR007/TCG007 (c,d).

886  
 887  
 888  
 889  
 890  
 891  
 892

893

(a)

(b)



894

895 **Figure 6.** Time history of acceleration modulus during Tohoku earthquake: measured data and  
896 numerical solution at the ground surface (a); reference bedrock signal and surface numerical  
897 solution (b), for case IBR007/FKS031.

898

899

900

901

902

903

904

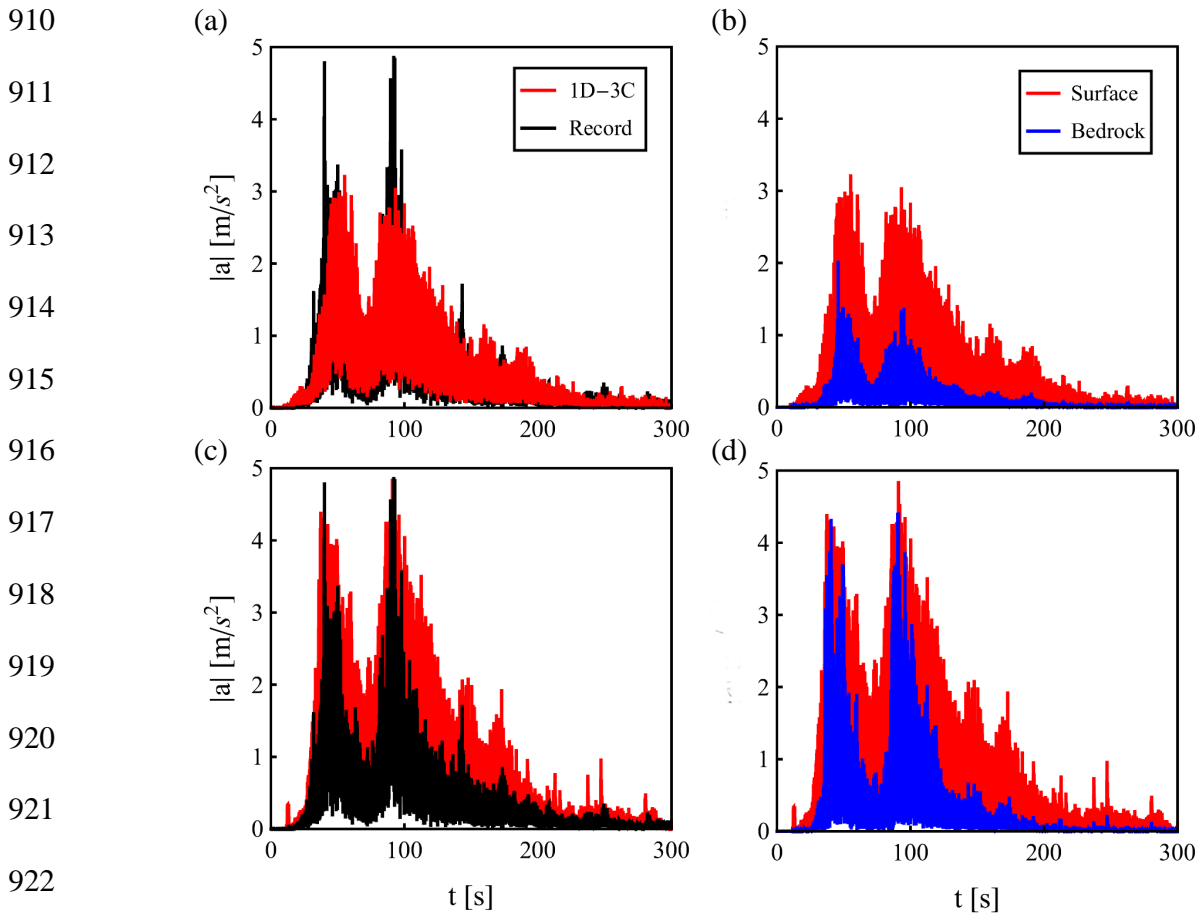
905

906

907

908

909



923 **Figure 7.** Time history of acceleration modulus during Tohoku earthquake: measured data and  
 924 numerical solution at the ground surface (a, c); reference bedrock signal and surface numerical  
 925 solution (b, d), for cases MYG010/IWT008 (a,b) and MYG010/MYG011 (c,d).

926

927

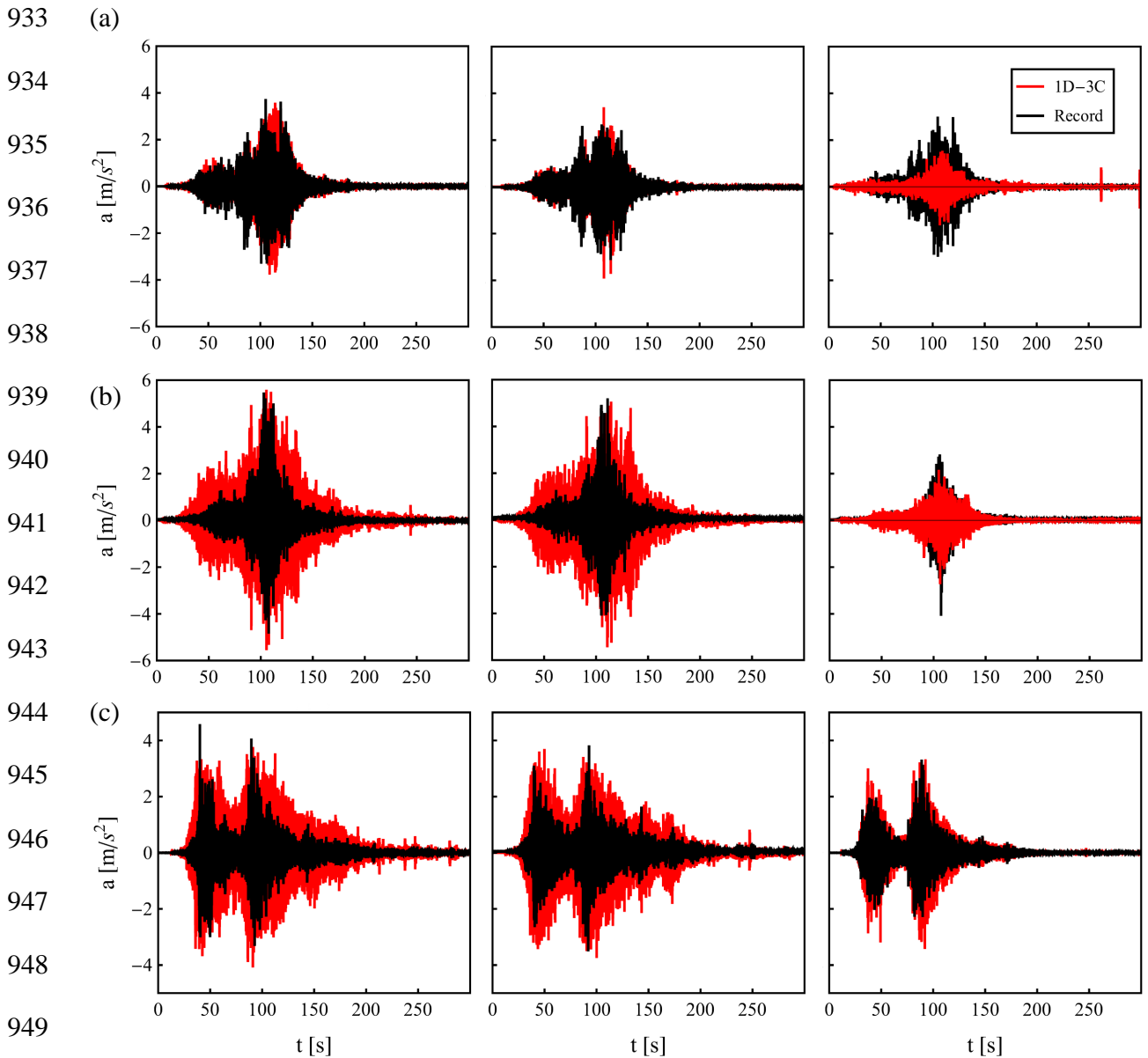
928

929

930

931

932



950 **Figure 8.** Three-component acceleration time history at the ground surface during Tohoku  
 951 earthquake: measured data and numerical solution in directions x (left), y (middle) and z (right),  
 952 for cases FKS011/FKS015 (a), IBR007/FKS031 (b) and MYG010/MYG011 (c).

953

954

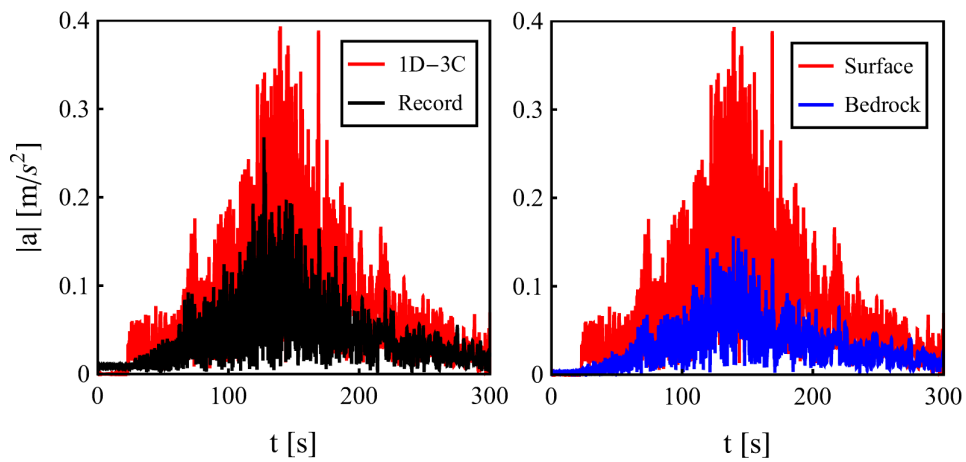
955



956

(a)

(b)



957

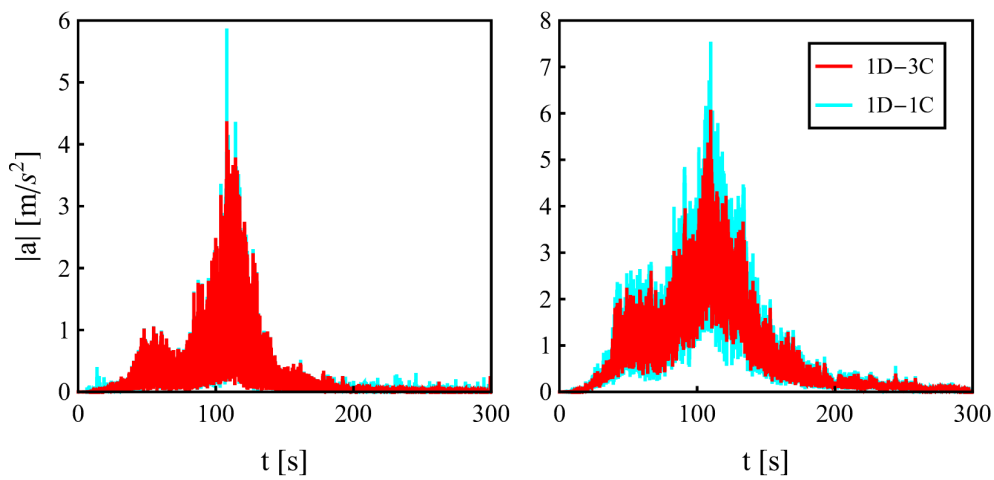
958 **Figure 9.** Time history of acceleration modulus during Tohoku earthquake: measured data and  
959 numerical solution at the ground surface (a); reference bedrock signal and surface numerical  
960 solution (b), for soil profile NIGH11.

961

962

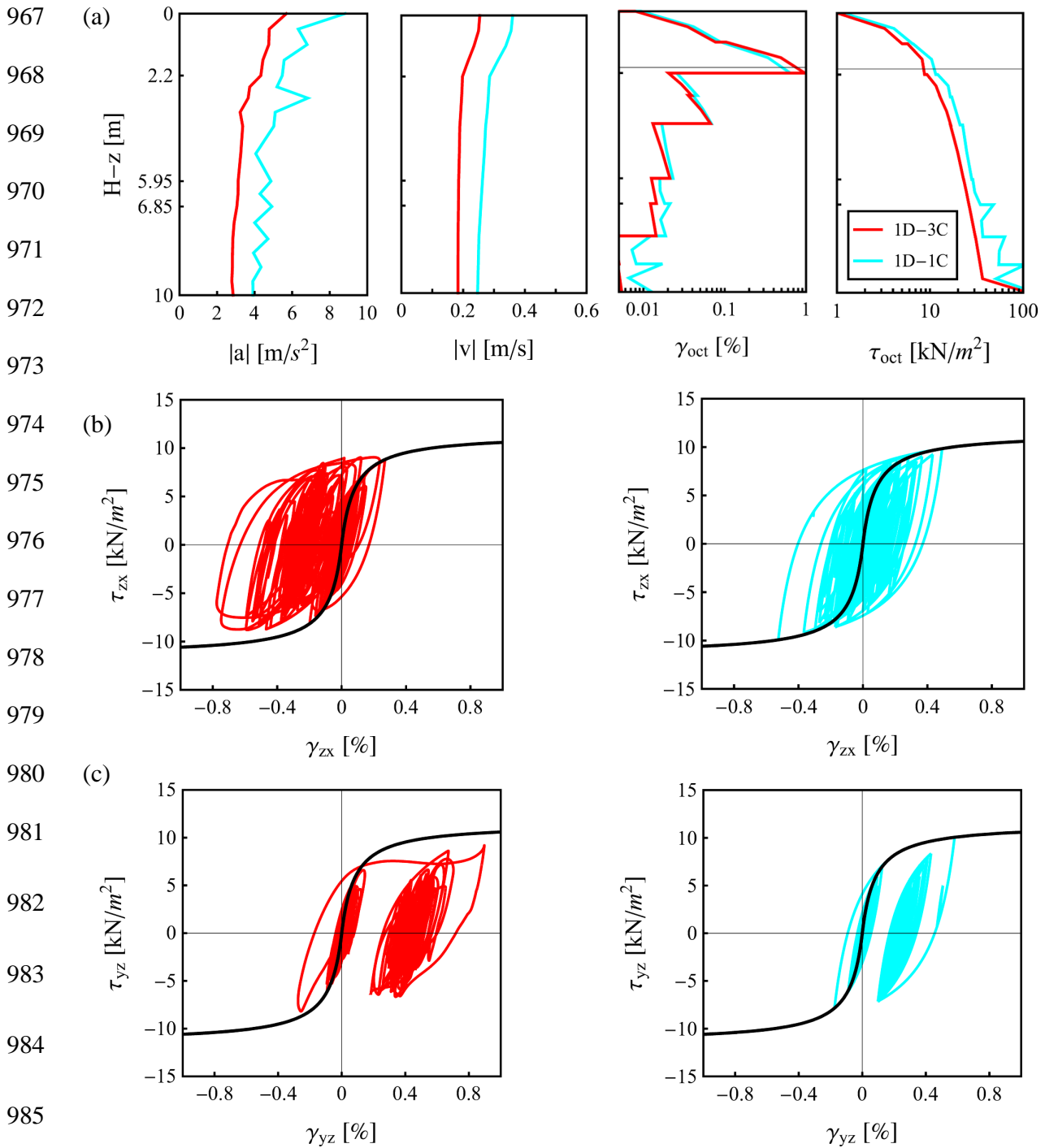
(a)

(b)

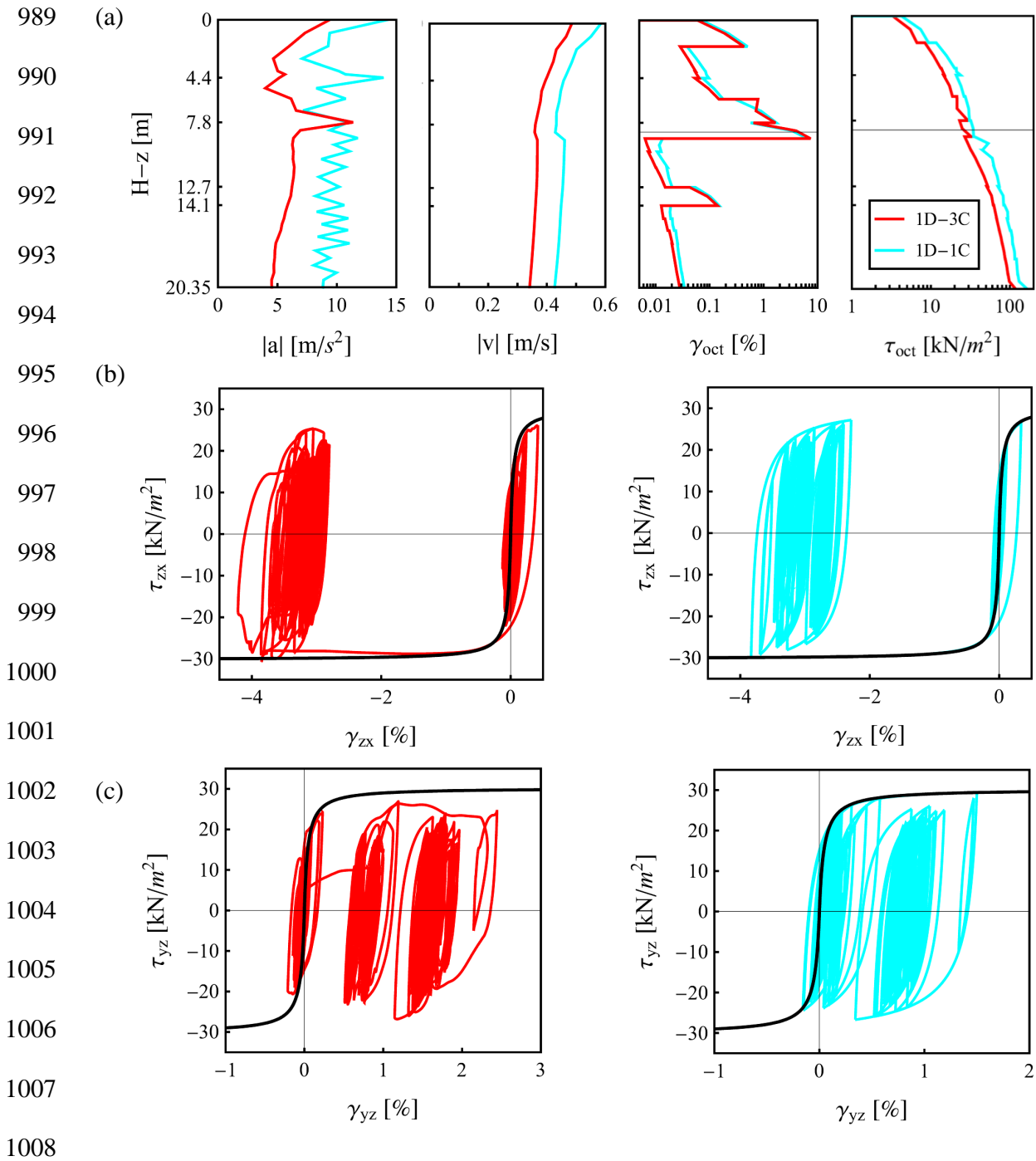


963

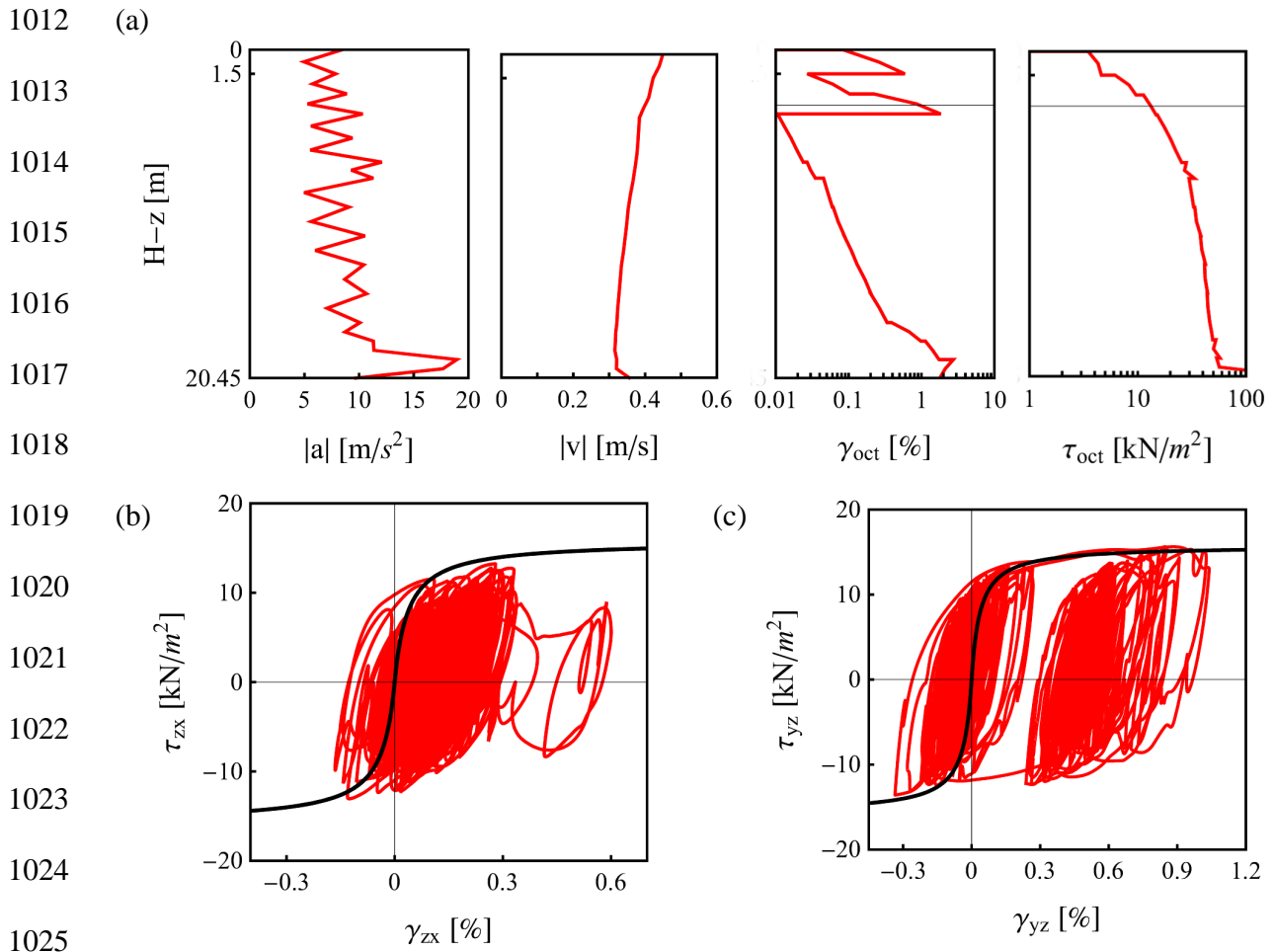
964 **Figure 10.** Time history of acceleration modulus at the ground surface during Tohoku  
965 earthquake: 1D-3C and 1D-1C numerical solutions for cases FKS011/FKS015 (a) and  
966 IBR007/FKS031 (b).



986 **Figure 11.** 1D-3C and 1D-1C seismic response during the Tohoku earthquake, for the case  
 987 FKS011/FKS015: profiles of maximum acceleration and velocity modulus, octahedral strain and  
 988 stress with depth (a); shear stress-strain loops at 2 m depth in x- (b) and y-direction (c).

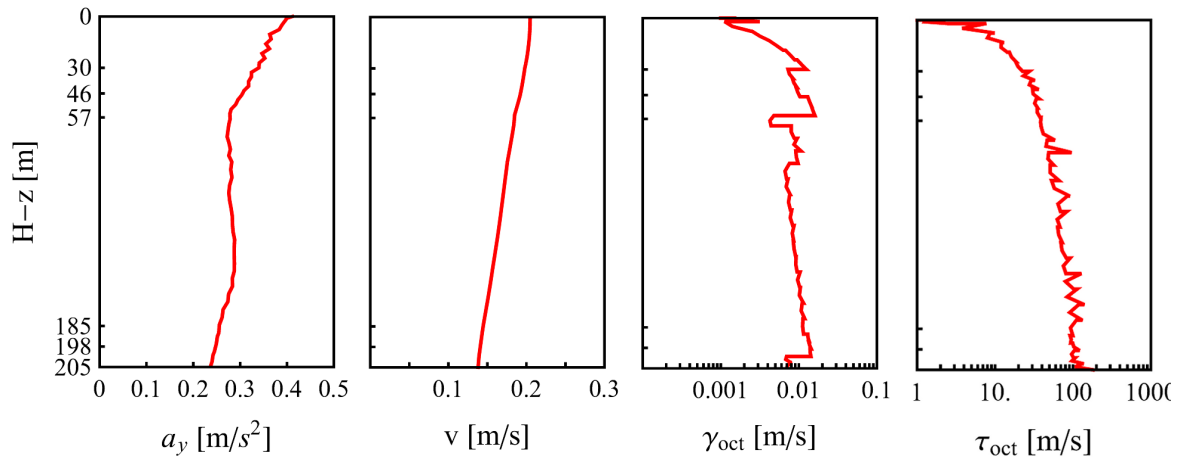


1009 **Figure 12.** 1D-3C and 1D-1C seismic response during the Tohoku earthquake, for the case  
 1010 IBR007/FKS031: profiles of maximum acceleration and velocity modulus, octahedral strain and  
 1011 stress with depth (a); shear stress-strain loops at 8.5 m depth in x- (b) and y-direction (c).



1026 **Figure 13.** 1D-3C and 1D-1C seismic response during the Tohoku earthquake, for the case  
 1027 MYG010/MYG011: profiles of maximum acceleration and velocity modulus, octahedral strain  
 1028 and stress with depth (a); shear stress-strain loops at 3.5 m depth in x- (b) and y-direction (c).

1029  
 1030  
 1031  
 1032  
 1033  
 1034



1035

1036 **Figure 14.** Maximum acceleration, velocity, octahedral strain and stress profiles with depth in  
 1037 soil profile NIGH11 during 2011 Tohoku earthquake.

1038

1039

1040

1041

1042

1043

1044

1045

1046

1047

1048

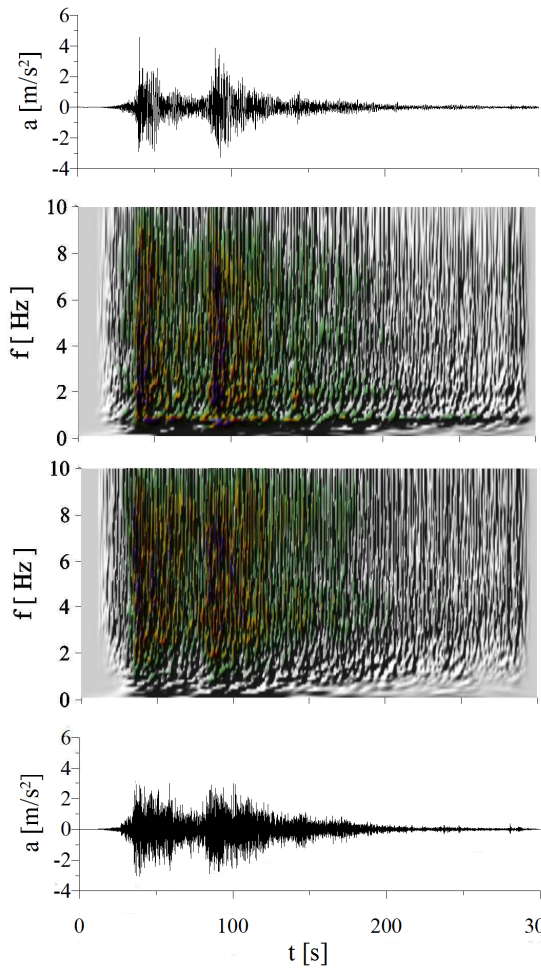
1049

1050

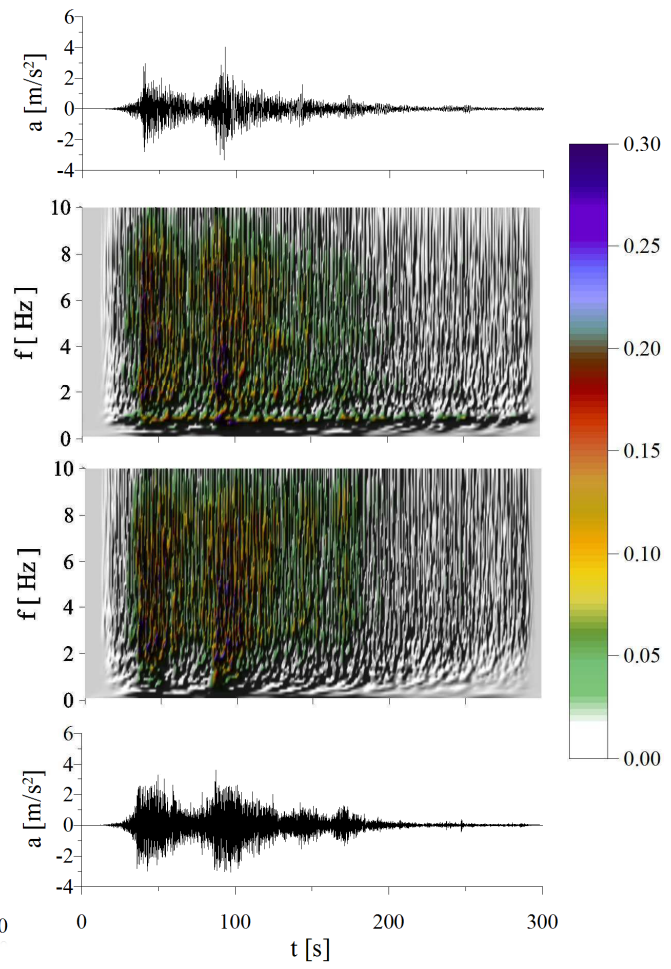
1051

1052

1053 (a)



(b)



1054

1055 **Figure 15.** Spectral amplitude variation with time and frequency at the ground surface, in  
1056 horizontal directions x (a) and y (b), during the Tohoku earthquake, evaluated using measured  
1057 acceleration (up) and computed acceleration (down) as input, for the case MYG010/MYG011.

1058

1059

1060

1061

1062